

12

Optical Properties: UV/Vis Diffuse Reflectance Spectroscopy and Photoluminescence

Thomas Berger¹ and Annette Trunschke²

¹Department of Chemistry and Physics of Materials, Paris-Lodron University of Salzburg, Jakob-Haringer-Strasse 2a, A-5020 Salzburg, Austria

²Department of Inorganic Chemistry, Fritz-Haber-Institut der Max-Planck-Gesellschaft, Faradayweg 4–6, D-14195 Berlin, Germany

12.1 Interaction of Metal Oxide Particle-Based Materials with Light

Many functional properties of metal oxide nanoparticles and nanoparticle-based materials are determined by the details of their interaction with electromagnetic radiation in the UV/Vis/NIR region. In many applications, the control of reflection, refraction, absorption, and scattering of the incident light is a prerequisite for systematically tuning the materials' optical properties and for triggering the physical or chemical response of a material to photoactivation, respectively. In this context, spectroscopic methods in the UV/Vis/NIR range can yield direct information on the materials' functional properties. Investigated materials' properties range from the optical properties of pigments (Chapter 22), to the absorption behavior of electrochromic films [1], the emission properties of down-conversion materials in lighting or display devices [2, 3], or the transmittance of metal oxide nanoparticle-based UV interference filters [4].

However, UV/Vis/NIR spectroscopic characterization methods are not limited to the direct investigation of functional materials' properties. Furthermore, they are extensively used to characterize relevant physicochemical features of highly dispersed metal oxide materials such as heterogeneous catalysts [5–8]. The energetic stimulation of electronic transitions in this type of material yields valuable information on the band gap transition in semiconductors, on point defects, bulk and surface excitons in semiconductors and insulators, as well as on the nature and chemistry of supported oxide moieties or adsorbed organic molecules. Some relevant transitions in the UV/Vis/NIR range together with the corresponding transition energies are summarized in Figure 12.1 and will be discussed in detail in Sections 12.3 and 12.4.

In general, light-material interaction processes are controlled both by the composition and by the structural properties of the material on different length scales.

The interaction of nonpolarized light with a thin layer consisting of homogeneously dispersed nanoparticles in a transparent matrix is schematized in Figure 12.2. Examples for such systems are blends of metal oxide nanoparticles and polymers as used in optical applications [4, 9, 10]. In terms of their optical properties very similar structures can be porous films of interconnected semiconductor oxide nanoparticles embedded in and penetrated by a liquid electrolyte as used in photoelectrocatalytic [11] and photovoltaic applications [12] or in electrochromic devices [1].

A light beam impinging on the material will be partially reflected from the surface (Figure 12.2). If the surface is smooth, the angle of reflection will equal the angle of incidence giving rise to

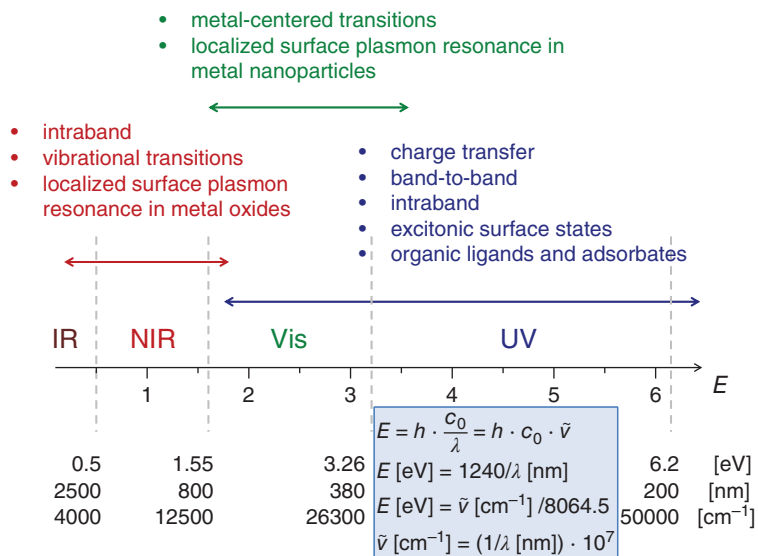


Figure 12.1 Types of electronic transitions in the UV/Vis/NIR range and formulas for the conversion of frequently used quantities (blue box). E is the energy in eV, h is the Planck constant, c_0 is the speed of light in vacuum, $\tilde{\nu}$ is the wavenumber of light in cm^{-1} , and λ is the wavelength of light in nm.

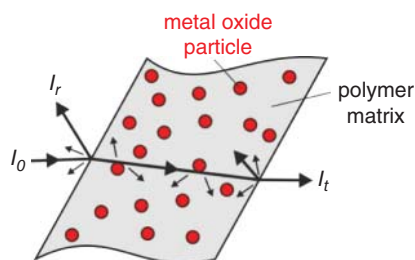
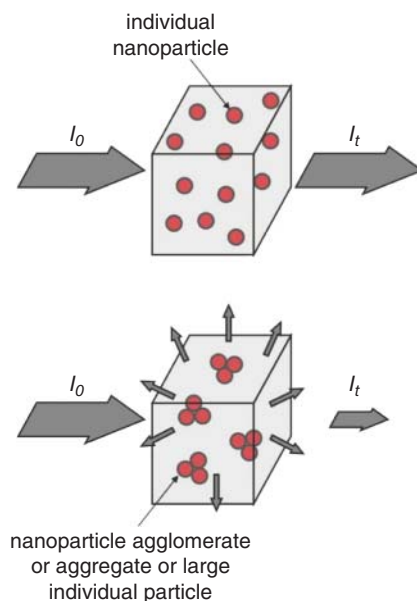


Figure 12.2 Absorption and scattering in metal oxide nanoparticle/polymer blends.

specular reflection. If the surface is rough, light will be reflected into various directions due to surface scattering (i.e. diffuse reflection). The refracted beam on the other hand will experience attenuation inside the material due to two different processes – absorption and scattering. The first process comprises the resonant excitation of electronic transitions in the material. The excited states may revert to the electronic ground states upon photon emission or energy dissipation into heat. The former process corresponds to photoluminescence (see Section 12.2.3). Elastic scattering processes, on the other hand, are not associated with a change of the photon energy. Instead, light is spread in directions away from the path of the refracted beam. The transparency of a material is defined as its ability to transmit incident light without being scattered, which makes fine details of an object situated behind the material (e.g. behind a film) perfectly discernible. Translucency, on the other hand, results from the scattering of transmitted light, which hampers image formation.

Since the refractive index of metal oxides is higher than the refractive index of organic materials, metal oxide particles act as strong scatterers in a polymeric matrix. The ability to strongly scatter visible light is the reason for the extensive use of submicrometer-sized TiO_2 particles as pigment in paints, coatings, plastics, paper, or inks [13–15]. However, as the size of the particles is reduced to the nanoscale and becomes much smaller than the wavelength of visible light, scattering is reduced and resulting nanoparticle/polymer blends are translucent or even transparent (Figure 12.3) [10].

Figure 12.3 Dependence of scattering loss on particle size. Source: Based on Demir, M.M. and Wegner, G. (2012). Challenges in the preparation of optical polymer composites with nanosized pigment particles: A review on recent efforts. *Macromolecular Materials and Engineering* 297 (9): 838–863 [10].



The loss of light intensity due to scattering can be estimated from Rayleigh's law

$$T = \frac{I}{I_0} = \exp \left[-\frac{3\phi_p x r^3}{4\lambda^4} \left(\frac{n_p}{n_m} - 1 \right) \right] \quad (12.1)$$

where T is the transmittance, I and I_0 are the intensities of the transmitted and incident light, respectively, λ the wavelength of light, ϕ_p the volume fraction of the metal oxide particles, x the thickness of the film, r the radius of spherical scatterers, and n_p and n_m are the refractive indices of the particles and the matrix, respectively. This formula was derived for nonpolarized light impinging on nonabsorbing and isotropically scattering particles with a radius r much smaller than the wavelength of light ($r < \lambda/20$).

Blending polymers with metal oxide nanoparticles allows for designing transparent or translucent composite materials with tunable optical properties such as high refractive indices (e.g. TiO_2 or ZrO_2) [3, 9, 10], luminescence (e.g. yellow-emitting phosphor $(\text{Y}_{1-x}\text{Ce}_x)_3\text{Al}_5\text{O}_{12}$ – YAG:Ce, ZnO, and semiconductor quantum dots of other materials) [2, 3, 9, 16], or selective UV shielding (ZnO , TiO_2 , ZrO_2 , CeO_2 , SnO_2 , SiO_2) [3, 4]. However, a strong scattering of visible light is associated with a loss in transparency of nanocomposites and limits their use in optical applications (Figure 12.3). As an example, ZnO/poly(methyl methacrylate) (ZnO/PMMA) blends featuring different volume fractions of ZnO particles are highlighted in Figure 12.4 [17]. While aggregates of loosely associated primary particles are embedded in the PMMA matrix without mutual contact at low volume fraction (Figure 12.4a), percolating networks of larger aggregates prevail at higher volume fractions (Figure 12.4b). Though ZnO does not absorb visible light, transmittance losses are observed at high volume fractions due to scattering (Figure 12.4c and d). Band-to-band transitions (Section 12.3.1) in ZnO (band gap width, $E_{\text{band gap}} = 3.3$ eV) give rise to light absorption at $\lambda = 350$ nm (Figure 12.4d).

The preservation of the materials' transparency upon the dispersion of metal oxide nanoparticles in the polymer matrix is therefore a key challenge. According to Eq. 12.1 intensity loss of transmitted light depends – for given particle loading and optical path length – on the following materials' properties:

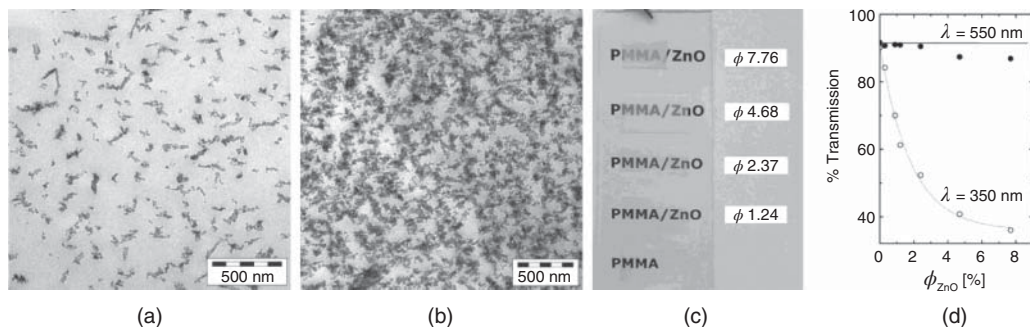


Figure 12.4 (a, b) Transmission electron micrographs of ZnO/PMMA blends featuring a volume fraction of ZnO particles (primary particle size: 12 nm) of (a) 1.24% and (b) 7.76%. (c) Photograph of 120 μm thick films made of ZnO/PMMA blends. The volume fractions of admixed ZnO are indicated in percent in the image. (d) Normal incidence transmission at 550 nm (full symbols) and 350 nm (open symbols) of 2 μm thick films as a function of the ZnO volume fraction. The solid line represents scattering losses as calculated by Eq. 12.1 assuming an invariant size of the scattering particles and the absence of multiple scattering. Deviations of experimentally determined values indicate that these assumptions are not fulfilled at high volume fractions. Source: Adapted with permission from Demir, M.M., Koyunov, K., Akbey, Ü. et al. (2007). Optical properties of composites of PMMA and surface-modified zincite nanoparticles. *Macromolecules* 40 (4): 1089–1100 [17]. © 2007, American Chemical Society.

- a) The size of the scatterers.
- b) The refractive index mismatch between particles and the surrounding matrix.

The high specific surface area of metal oxide nanoparticles promotes the often unwanted agglomeration and/or aggregation of primary particles. Due to the larger size of the secondary particles, they act as stronger scatterers (Figure 12.3). The homogeneous dispersion of nanosized primary particles in the matrix is therefore a key challenge for obtaining highly transparent blends and requires synthesis routes yielding individualized metal oxide nanoparticles and a subsequent embedding into a material upon prevention of agglomeration/aggregation. For this purpose several surface functionalization and stabilization approaches as well as *in situ* synthesis techniques have been developed [3, 18, 19].

Even for a dispersion of individualized metal oxide nanoparticles in the polymer matrix, significant scattering will be observed due to a refractive index mismatch between the individual material components. According to Eq. 12.1 scattering is suppressed only if the refractive indices are equal and index matching is achieved.

While for the design of polymer blends light scattering may be desired or undesired depending on whether one aims at opaque white or transparent films and coatings, characterization of particle powders relies on the analysis of scattered light. In this context, a phenomenon, which is completely neglected in Eq. 12.1, is multiple scattering. It corresponds to a situation, where an incident photon is scattered many times without absorption and before leaving the material. Multiple scattering is associated with an increased path length of light within the material and results in a stronger decrease or full annihilation of the transmitted light intensity (Section 12.2.2). Furthermore, for multiple scattering it is no longer possible to describe the directional distribution of the scattered light emerging from the material. Such effects prevail in the case of thick samples, where the scattering volume is large and the number of scatterers per unit path length is high. While multiple scattering eludes rigorous description, there exist phenomenological theories, which consider both scattering and absorption in related systems. These theories are important for the characterization of nanoparticle powders and will be discussed in detail in Section 12.2.2.1.

12.2 Spectroscopic Techniques

The broad application of UV/Vis/NIR spectroscopy in the field of oxide nanoparticles covers monitoring of chemical reactions during materials synthesis, the analysis of bulk and surface properties, and the investigation of processes at interfaces between nanoparticle surfaces and surrounding media. Photoluminescence spectroscopy is used in the investigation of emission properties of materials and in the analysis of surface and bulk defects. The diversity of research questions requires an adaptation of the experimental techniques with regard to the optical properties of the medium that contains the relevant analyte in order to minimize experimental errors. The medium can be:

- A homogeneous solution of molecular or supramolecular precursors.
- Transparent crystalline or vitreous solids and thin films.
- Colloids and slurries in the course of nucleation and growth or an already stabilized product.
- Polycrystalline or amorphous powders in vacuum or in contact with gas or liquid phase.

The most frequently applied techniques include transmission spectroscopy, diffuse reflectance spectroscopy (DRS) and photoluminescence spectroscopy. The application areas and principles of these measurement techniques will be explained briefly in the following.

12.2.1 Transmission Spectroscopy

Dilute solutions, thin films, transparent crystals, glasses, or composite materials are studied by transmission spectroscopy. The light passes through the homogeneous medium arranged perpendicular to the beam, either between two parallel windows of a cuvette in the case of a liquid, or as a self-supported sample in case of a solid as a layer, giving a defined optical path length, ℓ (in cm), (Figure 12.5). The measurement of the transmittance $T_\lambda = I/I_0 = f(\lambda)$ as a function of the energy of the incident light results in the absorption spectrum, where I and I_0 denote the radiation flux with and without the absorbing layer in the optical path. The Lambert–Beer law renders quantitative analysis possible (Eq. (12.2)). The absorption coefficient α in the unit cm^{-1} depends on the concentration c (in mol cm^{-3}) of absorbing species. For quantitative measurements the molar extinction coefficient ϵ in the unit $\text{l mol}^{-1} \text{cm}^{-1}$ is used. Please note that the spectral absorbance A_{10} is a dimensionless quantity and that the Lambert–Beer law is only valid in dilute solutions ($c < 0.01 \text{ mol l}^{-1}$) in which the absorbance is a linear function of the concentration of the absorbing species.

$$A_{10} = -\log_{10} \left(\frac{I}{I_0} \right) = -\log_{10}(T_\lambda) = \alpha \ell = \epsilon c \ell \quad (12.2)$$

The measured absorbance is not the true absorbance because of energy loss due to specular reflection at phase boundaries (window of the cuvette or surface of the transparent solid) and

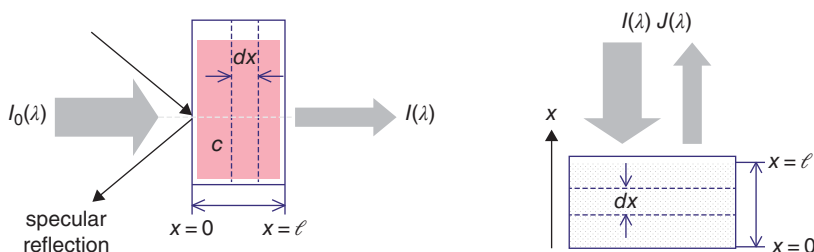


Figure 12.5 Optical pathway in transmission or specular reflection (left) and diffuse reflectance (right) spectroscopy.

12.2.2 Diffuse Reflectance Spectroscopy

Diffuse reflectance (DR) spectroscopy provides access to the absorption spectrum of a solid that scatters the incident light [6, 22, 23]. The optical phenomenon of diffuse reflection represents a limiting case in which a parallel beam of light that irradiates the surface of a solid material is uniformly reflected in all directions. The surface is an ideal matte surface in contrast to the polished surface of a mirror upon which the light is only regularly reflected (ideally specular reflection). Reflectance spectroscopy utilizing regular reflected light includes, for example, attenuated total reflection (ATR) spectroscopy [24] and infrared reflection absorption spectroscopy (IRRAS) [25]. In both techniques radiation in the mid-infrared is used. The diffuse reflectance approach applied in mid-infrared and UV/Vis/NIR implies that the angular distribution of the reflected light is isotropic, which is fulfilled if

- a powder contains particles with dimensions much greater than the wavelength of the incident light,
- *multiple* regular reflection occurs on crystal surfaces of randomly arranged particles, and
- repeated refraction and diffraction takes place inside the powder.

As outlined above, for smaller particles ($d \approx \lambda$), an isotropic distribution of the scattered radiation is not fulfilled when *single* scattering occurs on isolated particles as described by Mie's theory. However, in compact fine powders, where particles are in contact with each other, *multiple* scattering occurs. A large number of scattering particles, which are densely packed in a layer, provide on average an isotropic distribution of the diffusively reflected light. Provided the layer is thick enough, the light is not transmitted through the layer (Figure 12.5).

Selected absorption of the reflecting particles modifies the spectral composition of the diffuse reflected light. The absorption spectrum of a solid is accessible from the measurement of the diffuse reflectance, R , of a simultaneously scattering and absorbing powder. R is defined as the ratio of the diffuse reflected radiation flux J to the incident radiation flux I (Figure 12.5). The reflectance is measured as a function of the wavelength, λ , or the wavenumber, $\tilde{\nu}$, resulting in the reflectance spectrum $R = \frac{J}{I} = f(\lambda)$. The corresponding value in transmission spectroscopy is the transmittance T_λ (Eq. (12.2)). In analogy to absorbance curves (Eq. (12.2)), it is also common to plot $\log(1/R)$ as a function of the wavelength λ . $\log(1/R)$ is called the "apparent absorbance".

12.2.2.1 Kubelka–Munk Theory

Kubelka and Munk have shown that R depends exclusively on the ratio of absorption and scattering coefficients of the analyzed solid, but not on their absolute values [26]. R is, therefore, not proportional to the concentration of the absorbing species in the investigated material. Under certain experimental conditions, however, when the "Kubelka–Munk function" (also called "remission function") $F(R_\infty)_\lambda$ is valid, the separation of scattering and absorption coefficients is possible (Eq. (12.3)).

$$\frac{K_\lambda}{S} = \frac{(1 - R_\infty)^2}{2R_\infty} \equiv F(R_\infty)_\lambda \quad (12.3)$$

R_∞ is the diffuse reflectance of an infinitely thick, opaque layer of the sample, K_λ is the molar absorption coefficient and S is the scattering coefficient [26].

Layer thicknesses that fulfill the condition of R_∞ (i.e. opaque layer, no transmission) depend on the materials properties, which define scattering and absorption coefficients that again depend on the wavelength of the incident light, and the packing density [26]. Generally, sample thicknesses of 2–5 mm are sufficiently in accordance with R_∞ .

In Eq. (12.3), the scattering coefficient S is assumed to be independent of the wavelength. If this assumption is valid, the plot of $F(R_\infty)$ as a function of K_λ (if K_λ is known from independent transmission experiments for example by measurement of a colored glass in transmission and after pulverization in diffuse reflectance) yield a linear curve [27]. Considering the logarithmic form of the Kubelka–Munk function,

$$\log F(R_\infty)_\lambda = \log K_\lambda - \log S \quad (12.4)$$

the absorbance spectrum of a solid measured in transmission should only be displaced by $-\log S$ along the ordinate with respect to the $\log F(R_\infty)_\lambda$ spectrum while $K_\lambda \propto \epsilon c$ (see Eq. (12.2)). In particular, in the high-energy range of the spectrum, systematic deviations might be observed, which indicate that the assumptions made in the Kubelka–Munk theory are not always fulfilled in practice. Implications of these limitations on the analysis of nanostructured metal oxides will be discussed in Section 12.2.2.3.

12.2.2.2 Measurement of Absorption Spectra in Diffuse Reflectance

In a normal spectroscopic experiment applying a double-beam spectrometer, the diffuse reflectance of a sample, $R_{\infty, \text{sample}}$, can only be measured as the relative quantity, R'_∞ , in reference to a comparison standard (white standard), $R_{\infty, \text{standard}}$ (Eq. (12.5)).

$$R'_\infty = \frac{R_{\infty, \text{sample}}}{R_{\infty, \text{standard}}} \quad (12.5)$$

If $R_{\infty, \text{standard}} \equiv 1$, then the measured relative reflectance R'_∞ would correspond to the absolute reflectance R_∞ .

The absolute reflectance of the white standard must be known in the spectral range of interest. Ideal white standards reflect all incident light ($R_{\infty, \text{standard}} \rightarrow 1$) and exhibit no absorption ($K_{\text{standard}} \rightarrow 0$) in the entire range of energy, but in reality this is normally not completely fulfilled.

Absolute values, $R_{\infty, \text{standard}}$, of weakly absorbing standards have been measured by determining the wavelength dependence of the scattering coefficient, S [28]. For this purpose, white standards of variable layer thickness were measured in a black sample holder that exhibits apparent zero reflectance, R_0 (all light is transmitted or absorbed) [26, 28]. In the visible range, the scattering coefficient of samples consisting of equally sized particles is generally independent from the wavelength. However, over an extended wavenumber range $\tilde{\nu} = 10.000\text{--}40.000 \text{ cm}^{-1}$ (according to $\lambda = 1000 \text{ nm--}250 \text{ nm}$ and $E = 1.24 \text{ eV--}4.96 \text{ eV}$), the scattering coefficients of commonly used white standards, such as MgO, vary significantly in an approximate range of $500 \text{ cm}^{-1} \leq S \leq 1500 \text{ cm}^{-1}$. Due to the high scattering coefficient of MgO the condition of infinite thickness is fulfilled for sample thicknesses of 2–5 mm. In contrast, the very fine powder of fumed silica (e.g. Aerosil 200) exhibits small scattering coefficients in the visible range ($S = 10\text{--}50 \text{ cm}^{-1}$) and no absorption. Consequently, the incident light penetrates deeply into the silica (20–100 mm) and the condition of infinite thickness might not be fulfilled. Therefore, it is not recommended to use Aerosil powders as comparison standards [26]. Furthermore, in particular in the UV range, S of Aerosil 200 shows a distinct dependence on the wavenumber $S = \text{constant} \cdot \tilde{\nu}^{-\alpha}$, $\alpha = 3.2$ [28], which leads to a distortion of the remission function in the UV range compared to the true absorbance spectrum. The impact of such effects will be discussed in the next chapter.

In addition, due to the presence of trace amounts of unavoidable impurities, all white standards have also finite K values. Barium sulfate and freshly calcined magnesium oxide frequently used as white standards have been complemented today by polytetrafluoroethylene (PTFE) that exhibits improved chemical stability and $R_\infty > 0.9$ in the entire range between 250 and 2500 nm (<http://www.labsphere.com/site/assets/files/2553/a-guide-to-reflectance-materials-and-coatings.pdf>).

12.2.2.3 Experimental Limitations and Sources of Error

A true absorption spectrum can be determined when all assumptions and boundary conditions of the Kubelka–Munk theory are fulfilled. In practice, however, the measured remission function also depends on nature and morphology of the sample (particle size, particle shape, refractive index) and sample preparation. The influence of sample preparation (packing density, grinding, dilution) on the measured remission function is basically caused by

- (i) particle size and wavelength dependence of both the scattering and the absorption coefficients, and
- (ii) superposition of diffuse and regular reflection in the reflection of light at matte surfaces.

These complications render the quantitative analysis using diffuse reflectance spectroscopy more difficult. They also have implications on the intensity ratio of absorption bands and peak positions, systematic changes that should be taken into account when experimental data are compared to spectra simulated by theory. Some parameters that lead to distortion of the spectra are briefly described in the following. A detailed discussion is provided by the monograph of G. Kortüm [26].

- (i) The dependence of the scattering coefficient on the wavelength of the incident light has an impact on the measured remission function, which is less distinct for larger particles. However, in the case of larger particles, the spectrum can be compromised by regular reflection (complication (ii), see below). Grain sizes from 0.1 to 1 μm of particles in the powder sample or white standard represent a reasonable compromise. But in this size range, the scattering coefficient generally increases with the energy of the incident light, an effect that is associated with a decrease in the penetration depth. This means that a decreasing amount of material is analyzed with increasing energy of the light, which reduces the absorbed fraction of the incident radiation in the same direction. The resulting lower intensity of the absorption bands at higher excitation energies are reflected in a flattening of the spectrum towards the UV region and a distortion of the spectrum so that the relative band intensities are different from the relative band intensities in the true absorption spectrum. Hence, for a quantitative analysis one must determine the dependence of the scattering coefficient on the wavelength. Also, care should be taken when intensity ratios of absorption bands are compared with results from theory. An additional consequence of the energy dependence of S is a possible slight red shift of peak maxima that can be explained by the Kubelka–Munk theory (for details see Reference [26], p. 211). In heterogeneous materials such shifts can have an effect on the shape of the spectrum, meaning that shoulders appear or disappear depending on the sample preparation, for example, when the particle size distribution is changed by grinding. Furthermore, the loss of the precondition of an infinite layer thickness with changing scattering constant is an important phenomenon. If this condition is not fulfilled for a white standard, this leads to values of the apparent reflectance of the measured sample of $R > 1$.
- (ii) The relative contributions of diffuse and regular reflection in the diffuse reflected light depend on particle size, packing density, crystal morphology, refractive index, and absorbance of the solid. Variations in the relative contributions give rise to a loss of isotropic scattering and, thus, deviations from Kubelka–Munk theory. Regular surface reflections are mirrored by an observed decrease of the differences between peak minima and maxima. With increasing reflectance (decreasing absorption) the impact of regular reflection becomes less pronounced.

To circumvent the disadvantages outlined above, dilution of the sample with the white standard is recommended [26]. Dilution has the following positive effects:

1. The reflectance of highly absorbing samples can be adjusted to values $R'_\infty < 0.6$ to avoid deviations from the Kubelka–Munk theory.
2. The scattering coefficient of the mixture practically corresponds to the scattering coefficient of the pure white standard with the following implications:
 - 2.1. The calculation of the absorption coefficient directly from the remission function by using measured data of S for the white standard becomes possible.
 - 2.2. Contributions from regular reflection are cancelled out and an anisotropic scattering distribution is avoided.
 - 2.3. In high dilution the particle-size dependence of the absorption coefficient becomes negligible.

Reasonable care must be taken in the preparation of mixtures to achieve homogeneity. Dilution is feasible for studying the optical properties of metal oxides under ambient conditions. Dilution, however, becomes problematic when the oxides are investigated at elevated temperatures and in contact with gases. The diluent may undergo chemical reactions with the sample and the surrounding medium. Furthermore, alterations in the particle size may occur at high temperatures due to sintering or other chemical processes. Changes in $F(R_\infty)$ with temperature or composition of the medium are, therefore, not necessarily related to changes of K only. Therefore, interpretation of diffuse reflectance spectra measured *in operando* (i.e., while a catalyst is operating at high temperatures and in the presence of a gas phase) requires additional information obtained by complementary techniques. Related conclusions should be limited to the analysis of trends rather than to absolute figures.

12.2.2.4 Optical Accessories

Optical accessories for UV/Vis/NIR measurements in diffuse reflectance include integrating spheres, hemispherical mirrors, or fiber optics combined with cells that have been developed to analyze samples in specific environments.

In a classical DRS accessory, the sample is a part of the inner wall of a hollow sphere (integrating sphere, also called Ulbricht sphere or photometer sphere) coated with a material that is commonly used as a white standard, such as magnesium oxide, barium sulfate, or PTFE (in the NIR to mid-IR region, gold coatings are used as high reflectivity materials), (Figure 12.7, top left). The sphere collects the light diffusely reflected in and from all directions. Additional ports for light source, aperture to the detector(s) and a trap to extinguish regular reflected light (gloss trap) are placed in the wall of the sphere. The accessory is embedded in the optical path of a commercial UV/Vis spectrometer. Fast switchover between measurements in diffuse reflectance and transmission is therefore impossible. The fraction of the flux approaching the detector is small and corresponds at best to 1% of the incident flux [6].

Mirror optics make use of hemispherical mirrors, which direct the incident beam to the sample in a horizontal position and collect the diffusively reflected light. They can be placed directly into the sample compartment of the UV/Vis spectrometer (Figure 12.7, top right) (http://www.harricksci.com/sites/default/files/pdf/data_sheets/Data_Sheet_Praying_Mantis.pdf). Although the diffuse reflected light is collected over a smaller solid angle as compared with the integrating sphere and intensity loss at the mirrors (in total six pieces) has to be taken into account, the throughput of light is > 70% in the NIR. The response goes through a minimum at 825 nm of 30% due to mirror properties, reaches almost 50% in the visible range, and decreases finally to 30% in the UV region [6]. This type of accessory requires alignment of the mirror position and distance of sample surface to the hemispherical mirrors (height of the sample). The spectrum is sensitive with respect to sample height. Any change in the sample height between reference and

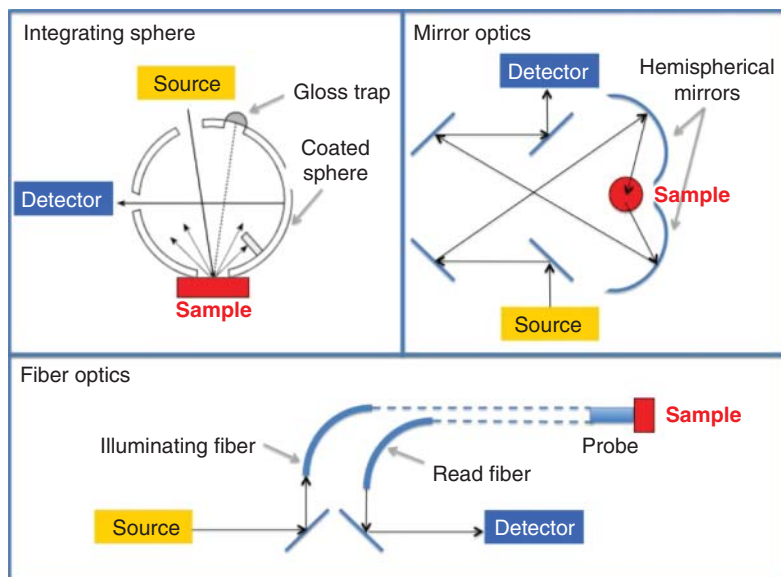


Figure 12.7 Illustration of the optical pathway in the various accessories applied in diffuse reflectance spectroscopy.

sample measurement and/or the sample volume, e.g. shrinking which may arise from thermal sample treatment, results in artifacts. Such artifacts, for example, correspond to steps in the spectra at one or two different wavenumbers. One step usually occurs at the energy position of lamp change from the UV range (deuterium lamp) to the visible region (tungsten–halogen or pulsed xenon lamps) between 300 and 350 nm. The other step is due to the detector change in conventional spectrometers from UV/Vis range (photomultiplier tube) to the NIR range (PbS detectors) around 800 nm. In addition, reflectance values > 1 may also result for this reason.

Fiber optics enable one to perform measurements on samples that no longer need to be located in the sample compartment of the spectrometer (Figure 12.7, bottom). The length of the fiber can be up to several meters. The beam is coupled out from the spectrometer using an adaptor and directed to the fiber head by total internal reflection within the fiber that is composed of silica. Generally, fiber bundles are used that illuminate the sample. In a typical arrangement, for example, 6 to 17 illuminating fibers surround one or two read fibers. The light diffusely reflected from the sample passes through the read fiber to the detector of the spectrometer. In special layouts, a white standard is integrated in the probe in order to correct fluctuations and drift from the light source by periodic measurements of reference spectra, increasing reliability in long-term measurements. A 30° angled window at a small distance from the fiber bundle tip serves to reduce specular reflection. Fiber heads that allow the measurement of solutions in transmission are also available. Apart from the above-mentioned advantages, the general disadvantage of measurements with fiber optics is that the incident light suffers from significant attenuation. This results in spectra that exhibit a lower signal to noise ratio as compared to measurements of the same sample and performed with mirror optics or integrating spheres.

12.2.3 Photoluminescence Spectroscopy

12.2.3.1 Principles of Photoluminescence Spectroscopy

Photoluminescence (PL) describes the process of light emission by a molecule or solid upon the transition from an excited electronic state that was previously populated by light absorption to

its ground state. PL spectroscopy is a highly sensitive method (e.g. modern fluorescence sensors for *in situ* chlorophyll analysis in water reach detection limits as low as $0.01 \mu\text{g L}^{-1}$ [29]) and has extensively been used for the characterization of metal oxide nanoparticle-based materials such as

- In studies on the emission properties of inorganic down-conversion materials [30–32].
- In the investigation of active sites in heterogeneous catalysis.
- In the elucidation of the reaction dynamics in catalysis and photocatalysis, respectively [7, 8].
- In addition, the PL properties of semiconducting metal oxides have received substantial attention in surface science studies [33, 34], where PL emission intensity variations were related as a diagnostic tool to measure band bending and surface potentials of semiconductor particles and related changes upon adsorption of charge-donating and -accepting molecules or exposure to UV light [34].

The principal components of a PL spectrometer are the excitation light source, a monochromator system at the excitation side, a sample compartment, a monochromator system at the emission side and the detector (Figure 12.8). For transparent samples, the emitted light is typically collected at 90° to the incident light beam, however, for particle powders or pellets, signals can be detected only in a front face geometry (Figure 12.8).

Emission spectra are recorded under or after electronic sample excitation by light absorption. The wavelength of the excitation light (λ_{exc}) must fulfill the resonance condition for an electronic transition in the sample

$$\Delta E = h \frac{c_0}{\lambda_{\text{exc}}} \quad (12.6)$$

and is fixed ($\lambda_{\text{exc}} = \text{const.}$) by means of the excitation monochromator. The wavelength-dependent intensity of the emitted light is then measured at the detector while scanning through the emission monochromator. The representation of the intensity of the emitted light as a function of its wavelength ($I_{\text{em}} = f(\lambda_{\text{em}})$) then gives the emission spectrum.

Excitation spectra are recorded by measuring the intensity of the emitted light (I_{em}) at a fixed wavelength ($\lambda_{\text{em}} = \text{const.}$) while scanning through the excitation wavelength (λ_{exc}) using the excitation monochromator. The excitation spectrum corresponds to the wavelength-dependent intensity of the emitted light ($I_{\text{em}} = f(\lambda_{\text{exc}})$) and resembles the information gained from absorption spectra provided (i) that sample absorption is weak ($A_{10} < 0.05$), (ii) that impurities are absent, and (iii) that the emission quantum yield does not change with the excitation wavelength [35].

PL measurements are associated with a significantly higher sensitivity than absorption measurements. Whereas the sensitivity of absorption spectroscopy is limited by the ability of the spectrometer to discriminate between two nearly equal light intensities (I and I_0 , see Eq. (12.2)),

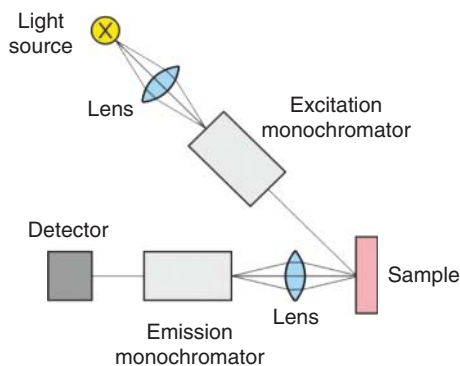


Figure 12.8 PL spectrometer in front face geometry.

PL measurements are limited only by the ability to detect light of low intensity levels. Due to the high sensitivity of PL spectroscopy, sample cells have to be made of high-purity materials such as Suprasil® glass.

In the absence of chemical reactions, the excited electronic state may revert to the electronic ground state upon photon emission (radiative decay) or upon energy dissipation into heat (non-radiative decay). Two different mechanisms can be involved in the radiative decay of the excited state. Fluorescence is a very fast emission process involving states with the same spin multiplicity (i.e. singlet–singlet transitions). Phosphorescence is associated with the forbidden transition between two electronic states with different spin multiplicity (i.e. triplet–singlet transitions) and is therefore characterized by longer lifetimes. Nonradiative decay processes of the excited state compete with emission and therefore affect the PL intensity. For solids, the probability of non-radiative decay depends on the ability of the host lattice to dissipate the absorbed energy converting it into heat. Sample cooling to low temperature may reduce the contribution of nonradiative processes by mitigating an effect known as thermal quenching and which manifests itself by a significant decrease of the luminescence efficiency above a certain temperature. From a technological point of view, temperature-dependent luminescence efficiencies may constitute a major problem for the application of down-conversion phosphors such as rare-earth doped photoluminescent materials (see Section 12.2.3.2) in white light-emitting devices as they give rise to an unwanted temperature-dependence of the spectral distribution of emitted light. Thermal quenching effects sensitively depend on the electronic properties of both the host material and the rare-earth dopants and models of different levels of sophistication have been developed to describe the underlying processes [36].

In this context, the quantum efficiency of photoluminescence (ϕ) is an important parameter for the characterization of an emitting species. It is defined as the ratio of the number of photons emitted to the number of photons absorbed and is given by

$$\phi = \frac{k_r}{k_r + k_{nr}} \quad (12.7)$$

Here k_r and k_{nr} are first order rate constants associated with the radiative decay (k_r) and all possible nonradiative decay processes (considered by a single rate constant, k_{nr}).

Steady state photoluminescence spectra are acquired upon continuous light exposure of the samples (using e.g. mercury or xenon arc lamps). The use of pulsed light sources (such as flash lamps, pulsed light emitting diodes, or lasers) allows for the measurement of time resolved PL spectra or PL decay profiles and thus the identification of the lifetime (τ) of the emitting species. The lifetime of the excited state, which corresponds to the average time the system spends in the excited state prior to the return to the ground state, is then expressed as

$$\tau = \frac{1}{k_r + k_{nr}} \quad (12.8)$$

12.2.3.2 Inorganic Luminescent Particles

Nowadays the most commercially important application of luminescent materials is in solid-state lighting devices based on blue and near-UV light-emitting diodes (LEDs) [37]. Luminescent materials are used as downconverters, which absorb the blue/UV light of the LED and emit in the visible spectrum. Current commercial down-conversion materials are micrometer-sized phosphor particles composed of an inert host lattice, usually a wide band gap material (e.g. oxides, nitrides, and sulfides) and a small amount of a dopant ion (also referred to as an activator) as the luminescent center (Figure 12.9) [2]. Typical dopants are transition metal elements or rare-earth elements such

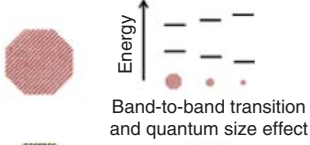

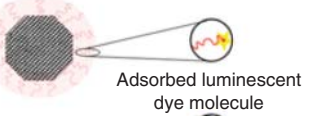
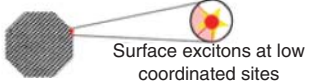
Type of Particle Luminescence	Origin of Luminescence Effect	Particulate Materials	Materials specific Requirements and Challenges
Quantum dots	 <p>Band-to-band transition and quantum size effect</p>	Semiconductors	Complex Synthesis, adjustment of surface composition, toxicity,...
Doped particles	 <p>Luminescent dopant ions</p>	Luminescent rare earth metal dopants inside inorganic hosts	Dopant solubility in the host with desired oxidation state
Organic-inorganic nanocomposites	 <p>Adsorbed luminescent dye molecule</p>	Ionic Insulators	Stability against abrasive molecule detachment
Surface excited states on particles	 <p>Surface excitons at low coordinated sites</p>	Ionic Insulators	Control over surface and interface properties

Figure 12.9 Schematic illustration of different types of photoluminescent inorganic nanoparticles, nature of associated photoluminescence emission and related materials challenges. Source: Figure reprinted from Sternig, A., Bernardi, J., McKenna, K., and Diwald, O. (2015). Surface-specific visible light luminescence from composite metal oxide nanocrystals. *Journal of Materials Science* 50 (24): 8153–8165 [39] Springer.

as Ce^{3+} or Eu^{2+} (Section 12.3.2.1). In some wide band gap semiconductors, significant luminescence can even be observed in undoped materials due to the presence of intrinsic defects. To reduce optical scattering losses and improve performance, there has been a drive to reduce particle size. However, surface defects in nanocrystalline rare-earth-based phosphor particles have been found to quench the emission intensity [38]. Consequently, there is a great deal of interest in exploring alternative luminescent materials for lighting applications. A brief overview of the types of inorganic luminescent particles currently in use or in development is given in Figure 12.9.

The different types of down-converting luminescent particles differ both in terms of the materials used and the nature of the luminescence effect. While phosphors feature localized luminescent centers (at dopant ions in the host lattice), absorption and luminescence in quantum dots involve transitions between electronic states, which are extended throughout the particle volume [2]. The luminescence energies can be easily tuned by varying the particle size and shape (Section 12.3.1.2) and they exhibit a very high quantum yield.

Organic–inorganic nanocomposites (compare Section 12.4.2) are composed of a luminescent organic dye that is attached to or incorporated in the inorganic nanoparticle [40]. Chemical and thermal stability issues as well as materials deterioration via leaching of the luminescence component, however, are continued challenges in the development of this class of material.

Nanocrystalline particle systems of pure and composite alkaline earth oxides have been proposed as a new class of down-conversion material for lighting applications [32, 39]. The luminescence in these materials is associated with low-coordinated surface or interface features (Section 12.3.1.3). Therefore, as particle size is reduced, quantum yield is improved and multiple scattering is minimized. While these materials show potential for applications such as down-conversion materials with adsorption-dependent optical properties [32], additional processes, which compete with photon emission and impact on the lifetime, the quantum efficiency, and thus the PL intensity have to be considered. In this context, photoluminescence quenching by O_2 is of particular importance. On highly dispersed alkaline earth metal oxide powders photoluminescence is observed only

under high vacuum conditions, whereas admission of molecular oxygen leads to photoluminescence quenching. Such behavior results from a weak interaction between molecular oxygen and the emission centers in their excited state (collisional quenching) leading to alternative nonradiative deactivation pathways. For such deactivation paths to be active, emission centers have to be located at the particle surface. The reversibility of the interaction between emission centers and molecular oxygen results in the full recovery of the emission intensity upon the reestablishment of high vacuum conditions [8].

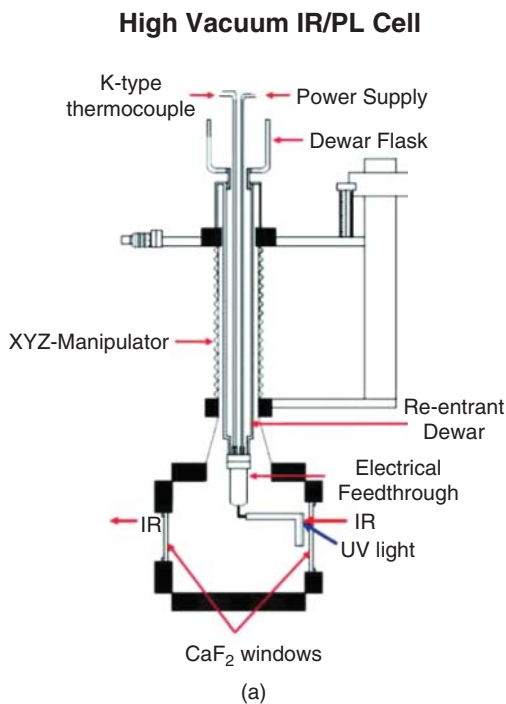
12.2.4 *In Situ* Cells and Measurement Configurations

Cells have been developed to analyze the synthesis of metal oxides, their bulk and surface structure under well-defined conditions with respect to temperature and gas atmosphere, as well as the dynamic response of electronic properties to changes in the atmosphere by UV/Vis/NIR spectroscopy. A multitude of technical solutions have been reported and general design issues have been described in detail previously [5, 41, 42].

Yates and coworkers developed a dedicated sample cell for measurements combining PL with FTIR surface spectroscopy on semiconductor oxide powders (Figure 12.10) [34]. PL emission intensity variations were used as a diagnostic tool to measure band bending and surface potentials of the semiconductor particles and related changes upon adsorption of charge-donating and charge-accepting molecules or upon exposure to UV light. The high-vacuum cell could be moved between an IR spectrometer and a PL spectrometer. The stainless-steel IR/PL vacuum cell contained two CaF₂ windows that were used for IR and PL measurements, respectively. The powdered TiO₂ sample was pressed into a tungsten grid and the closely spaced grid wires in the powdered sample allowed uniform temperatures to be achieved across the sample in a temperature range of 87–1000 K.

The cells applied in UV/Vis/NIR spectroscopy vary depending on the measurement technique, i.e. the optical accessories (Figure 12.7). The major challenge in *in situ* spectroscopy using integrating spheres is that the sample is a part of the wall of the sphere and any contact of the sphere with a specific gas atmosphere (the reaction medium in catalysis for example) or high temperature in *in situ* measurements needs to be avoided to protect the coating from damage. Cells include a quartz window, which is placed at the sample port of the sphere [43]. The sample powder is pressed against the window or pellets are used with a thickness of a few millimeters. Measurements in flowing gas at elevated temperatures are feasible when efficient cooling of the sphere is ensured. However, due to the cooling, temperature gradients close to the intersection between sample window and sphere may occur. Condensation on the sphere walls in low-temperature experiments is avoided by using double windows with the slit between the windows being evacuated. Gas phase contributions, particularly important in NIR measurements, can be neglected due to the close contact between sample and window. On the other hand, the small distance may cause pressure drops when operating in gas flow.

Cell designs for mirror optics are commercially available. The combination of the accessory with environmental cells is comparatively easy, because of the horizontal arrangement and the present distance of the sample holder to the mirrors. The sample is located in a sample cup, which is arranged below the spherical mirrors. The bottom of the cup consists of a mesh or frit making gas flow through the sample bed possible. The cells are equipped with ports for evacuation or introducing gases. The sample cup accommodates 50–250 mg of the powder depending on crystallographic and packing density of the material meaning that the requirements with respect to sample mass are lower compared to cells designed for integrating spheres. A cap (also called “dome”) is applied



Sample Holder

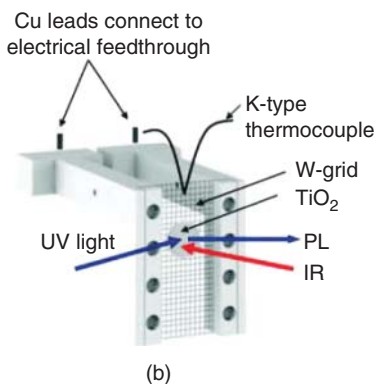
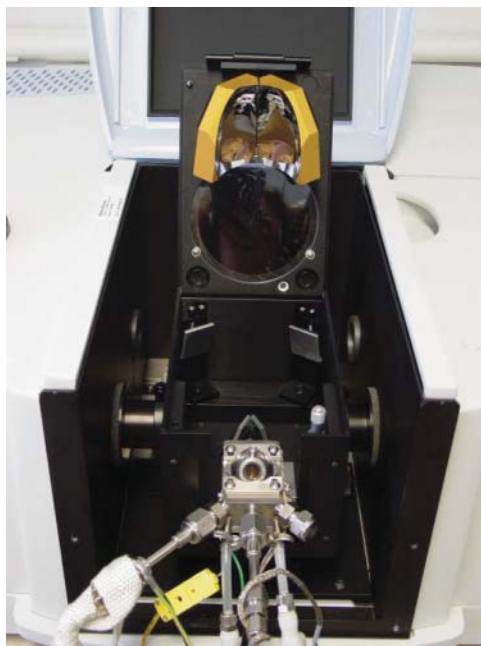


Figure 12.10 (a) Stainless steel IR/PL high-vacuum cell for PL and FTIR measurements. (b) Sample holder with clamped tungsten grid and pressed-powder semiconductor oxide disk. Source: Reprinted from Stevanovic, A., Büttner, M., Zhang, Z., and Yates Jr., J.T. (2012). Photoluminescence of TiO_2 : Effect of UV light and adsorbed molecules on surface band structure. *Journal of the American Chemical Society* 134 (1): 324–332 [34]. © 2012, American Chemical Society.

to seal the reaction chamber. The dome is equipped with windows for incident and diffuse reflected light. Window material is pure fused silica (Suprasil[®]), similar to the material used for cuvettes applied in transmission and PL spectroscopies. For measurement in the NIR region quartz glass that contains only a reduced number of OH groups is required as an optical material. Similar cells are available to perform Raman or infrared spectroscopy (Figure 12.11), which allows comparable measurements by just changing the cap, which is necessary to take into account differences in the optical pathways and to adopt the window material to the energy of radiation. Simultaneous implementation of a complementary spectroscopic technique by coupling in another beam, for example X-rays, is in principle possible as shown for diffuse reflectance infrared spectroscopy [44]. Commercial cells feature quite flexible conditions covering applications that range from

Figure 12.11 Harrick Praying Mantis™ accessory for diffuse reflectance UV/Vis/NIR spectroscopy with a high temperature reaction chamber that allows *in situ* and *operando* experiments in defined gas atmospheres.



vacuum (133 μPa) to 3 MPa pressure in flowing gases. The temperature is variable between low temperature (100 K) [45] and 1073 K [46, 47]. High temperature measurements are problematic in the near-infrared because NIR detectors are sensitive to the thermal radiation, which might cause high background noise and detector overflow. The sample is heated from the bottom and ports are available that allow gas phase analysis by gas chromatography or mass spectrometry. Major disadvantages of commercial cells for mirror optics are (i) linear temperature gradients in the region between the bottom of the sample cup where the heating cartridge is located and the top where the spectroscopic measurement is performed as well as (ii) radial temperature gradients, (iii) large dead volumes, and (iv) different fluid dynamics in the cell compared to common fixed bed tubular reactors in particular the possible bypass of a large fraction of the flowing gas [23, 48]. Furthermore, sample volume shrinking during thermal treatment can lead to changes in the height of the sample that may lead to artifacts and finally to a loss of the signal.

Application of fiber optics renders measurement under realistic conditions of catalytic reactions over heterogeneous catalysts possible. The fiber head is integrated in the reactor in which the sample is treated under the conditions of the application [49]. The maximum temperature in standard probes is limited normally to 473 K, but custom-made versions are available that allow measurements at higher temperatures [49–51].

Operando measurements in electrochemistry are frequently performed in transmission mode applying transparent conducting oxide materials such as indium tin oxide (ITO) as support to immobilize the catalyst [52–54]. Optical transparency and conductivity of materials allow simultaneous UV/Vis and electrochemical measurements that address charge transfer and related chemical transformations of the electrode material. Limits of the method include possible leaching of catalyst components into the electrolyte in the case of physical immobilization of the sample, or altered and sample unspecific charge transfer and conductivity in the case of covalent immobilization.

12.3 Types of Transitions

UV/Vis/NIR spectroscopy covers absorption of electromagnetic radiation in the energy range of approximately 5–0.5 eV (Figure 12.1). It can occur as a result of transitions between

- the energy states of outer shell electrons in atoms or ions,
- occupied and unoccupied molecular orbitals in molecular systems,
- or filled and empty electronic bands in solids.

The intensity of the absorption band corresponds to the absorption coefficient and reflects the extent of charge redistribution in the material upon interaction with the electromagnetic wave, i.e. the change of the electric dipole moment associated with the transition. An electronic transition is allowed when the transition dipole moment integral is nonzero. The transition dipole moment includes the wavefunctions of initial and final states and the dipole moment operator. According to the orbital or Laporte selection rule, the parity of an electric dipole transition has to change with the consequence that electronic transitions within similar atomic orbitals, such as $s \rightarrow s$, $p \rightarrow p$, or $d \rightarrow d$ in free atoms and many transitions in molecules with a center of symmetry are forbidden. In addition, the spin multiplicity of the involved levels must not change ($\Delta S = 0$; spin selection rule). Breaking the selection rules occurs by vibronic coupling, spin–orbit coupling, and exchange interactions meaning that forbidden transitions are observable, but the intensity is generally weak.

The fine structure and shape of absorption bands are determined by coupling with vibrational and rotational transitions in molecular systems and lattice vibrations in solids (electron–phonon coupling) and, are hence influenced by the measurement temperature.

The interpretation of absorption spectra of metal oxides and metal oxide precursor species requires the knowledge of their electronic structure. In the simplest case, metal oxides are considered as completely ionic compounds composed of negatively charged O^{2-} ions that surround positively charged metal cations M^{n+} . The lattice energy in this idealized view would result from purely electrostatic interactions of point charges (Madelung potential). However, considerable covalent contributions have to be taken into account since the covalent contributions to the metal–oxygen bonds depend on the position of the metal in the periodic table, its oxidation state, and coordination symmetry [55]. Charge transfer from the occupied oxygen 2p orbitals to empty $(n - 1)d$ or ns metal orbitals and overlap of atomic orbitals determine binding energy and width of the electronic band structure. The latter is also influenced by the bulk and surface defect chemistry of the metal oxide. The electronic properties of metal oxides determine their physical properties [56]. The electronic structure can be probed by optical characterization [57, 58].

The smallest building unit of a metal oxide is the metal atom surrounded by oxygen atoms in the first coordination sphere in different coordination symmetry including tetrahedral, octahedral, square planar, penta-, square- or trigonal (bi-) pyramidal, and cubic arrangements. More extended structures arise from connecting the metal-centered polyhedrons in different ways by sharing corners, edges, or faces resulting in an enormous variety that is specific to the structural chemistry of oxides and related compounds [59–61]. Metal–oxygen polyhedrons appear in molecular form during synthesis of metal oxides: examples are solvated cations, such as hexaquo complexes in water or polycations and anions formed by hydrolysis and condensation in solution. Small metal–oxygen complexes serve as building blocks in the assembly of structural motifs (secondary building units (SBU)) [62], and more extended structures [63–65]. Isolated metal oxide species anchored on the surface of a carrier oxide in functional materials such as metal oxide catalysts can be regarded as molecular units that correspond to a limiting case of extended 2D surface layers (Figure 12.12) [66, 67]. Vanadium oxide species supported on titania applied as catalyst in

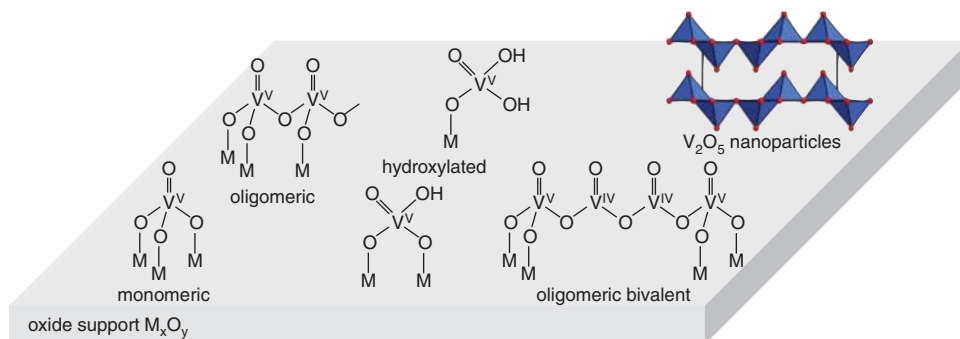


Figure 12.12 Some possible 2D surface structures of vanadium oxide species with vanadium in the highest oxidation state V^{5+} and with mixed valence V^{5+}/V^{4+} anchored on the surface of metal oxides M_xO_y , such as SiO_2 , Al_2O_3 , or TiO_2 . At high vanadium oxide loading 3D vanadium oxide nanoparticles can be formed.

selective catalytic reduction (SCR) of NO_x emissions with ammonia or urea from power plants or combustion engines in mobile applications belong to this class of materials.

In combination with theory, UV/Vis/NIR spectroscopy gives access to information concerning structure and dynamics of metal oxides or an absorbing center by investigating light absorption phenomena in the high energy UV/Vis (5–2.5 eV), visible (3.5–1.5 eV), and near-infrared (1.5–0.5 eV) regions (Figure 12.1). In the following, the various energy domains will be discussed separately.

12.3.1 UV Region (5.0–2.5 eV)

The highest energy, which is reliably measurable with standard laboratory spectrometers, common DR accessories, and white standards, corresponds to approximately 5 eV. One reason for this limitation is the absorption of molecular oxygen (O_2) in the air at $\lambda < 245$ nm. Measurements at higher energies require the purging of the spectrometer or vacuum systems. Absorption in the high-energy range between 5 eV and 2.5 eV contains:

- (i) Transitions in molecular systems from occupied molecular orbitals at donor atoms, i.e. the oxygen ligands of a metal oxide complex to empty molecular orbitals at acceptor atoms, i.e. the central transition metal atom of a complex (*charge transfer (CT) transitions*).
- (ii) *Band-to-band transitions* in semiconductors with a band gap width, $E_{\text{band gap}}$, of $E_{\text{band gap}} > 3$ eV for white materials, $1.5 \text{ eV} < E_{\text{band gap}} < 3$ eV for colored materials, and $E_{\text{band gap}} < 1.5$ eV for dark black materials in analogy to charge-transfer transitions in molecular systems. The transitions occur from the top of the filled valence band (having primarily oxygen 2p character) into the empty conduction band (made of antibonding orbitals that result from metal–oxygen interaction).
- (iii) Transitions from the filled valence band of materials with band gaps $E_{\text{band gap}} > 3$ eV into electron states within the band gap of the solid and associated with defect-induced *excitons* (electron e^- /hole h^+ pairs).
- (iv) Transitions in organic molecules from occupied bonding (σ , π) and nonbonding (n) molecular orbitals to unoccupied antibonding molecular orbitals (σ^* , π^*) [68]. These spectroscopic transitions are typically observed in *organic ligands* of metal oxide precursor complexes or in *adsorbates* on the surface of metal oxides that are in contact with organic media.

12.3.1.1 Charge Transfer (CT) Transitions

Charge transfer transitions occur in molecular systems, in which the highest occupied molecular orbital (HOMO) is mainly located at a donor atom and the lowest unoccupied orbital (LUMO) is predominantly located at an acceptor atom. The transition from HOMO to LUMO is called a charge transfer transition, it is Laporte allowed and, when $\Delta S = 0$, it produces absorption bands of high intensity.

One prominent example is the intense color of the permanganate ion MnO_4^- that is caused by such a charge transfer from the oxygen ligands to the central Mn ion in which the formal oxidation state of Mn (d^0 , formally 7+) decreases formally by one unit. The HOMO of the permanganate ion is mainly composed of oxygen 2p orbitals, the LUMO consists predominantly of Mn 3d contributions. The transition from HOMO to LUMO is called ligand-to-metal charge transfer (LMCT). Conversely, in some metal carbonyls with high-lying empty ligand orbitals and occupied orbitals with predominant metal d character, metal-to-ligand charge transfer (MLCT) occurs. Metal-to-metal charge transfer (MMCT) is observable in heteronuclear complexes.

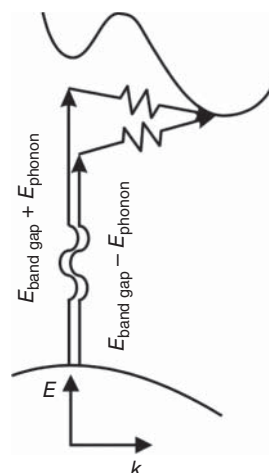
Generally, charge transfer bands are determined by the nature of the ligands and the central atom, as well as the oxidation state of the central atom and its coordination geometry. The optical spectrum therefore provides access to geometric and electronic structural information of molecular systems, but may also be useful in determining the local structure of isolated functional species, such as metal oxide clusters on the surface of oxides [66]. Intraligand transitions may also be of charge-transfer type, such as the NO_3^- band at 300 nm. Transitions in organic molecules acting as ligands or being adsorbed on the surface of metal oxides will be discussed separately (see Section 12.3.1.4).

12.3.1.2 Band-to-Band Transitions

Band-to-band transitions in semiconductor metal oxides are responsible for the absorption edge that can be observed for these materials in the near-UV/Vis range [5, 6, 8]. Light absorption occurs once the energy of the excitation light exceeds the band gap energy of the semiconductor, which corresponds to the energetic separation between the highest level in the valence band and the lowest level of the conduction band. Band-to-band transitions can be classified as direct or indirect. For direct semiconductors the energetic minimum of the conduction band and the maximum of the valence band are located at the same position in the reciprocal space (i.e. as expressed by the same wavevector, k). In an indirect semiconductor, the position of the lowest conduction band edge is shifted away from the highest valence band edge at the center of the respective Brillouin zone (Figure 12.13). The fundamental band-to-band transition, therefore, requires a change in both energy and momentum and is accompanied by the emission or the absorption of a phonon, which provides the change in momentum. The energy of the absorbed photon thus differs from the band gap energy ($E_{\text{band gap}}$) by the energy of the phonon (E_{phonon}). In the case of indirect semiconductors, both the fundamental absorption as well as the respective emission are much weaker in intensity than in direct semiconductors.

Upon electron excitation an unoccupied state, which corresponds to a positive hole in the valence band, is generated. This exerts an electrostatic force on the excited electron and may lead to the formation of an electron-hole pair, a so-called exciton. The attraction between electron and hole gives rise to additional electronic states in the band gap. Consequently, transitions at energies lower than the threshold energy for direct or indirect band-to-band transitions can be observed. In semiconductors exciton binding energies are typically small resulting in the ionization of the electron-hole pairs. Thus, corresponding optical transitions merge with the direct or indirect band-to-band transitions. In insulators, however, excitons can be tightly bound, which

Figure 12.13 Phonon assisted transitions in indirect semiconductors.



leads to appearance of discrete bands at energies below the band-to-band transition threshold (see Section 12.3.1.3 below).

Assuming that the scattering coefficient of semiconductor oxide particle powders does not change significantly in the spectral range where the band-to-band transition threshold is located, the band gap energy can be estimated from the Kubelka–Munk function, $F(R_\infty)$. For this purpose, a modified Kubelka–Munk function $[F(R_\infty) \cdot h\nu]^{1/n}$ is calculated and represented as a function of the excitation energy, $h\nu$, according to

$$[F(R_\infty) \cdot h\nu]^{1/n} \propto h\nu - E_{\text{band gap}} \quad (12.9)$$

with $n = 1/2$ for direct allowed transitions and $n = 2$ for indirect allowed transitions [6, 155]. The x -axis intercept, which is obtained upon extrapolation of the linear part of the resulting curve, then represents $E_{\text{band gap}}$. This procedure is illustrated for an anatase TiO_2 nanoparticle powder in Figure 12.14.

When the size of the semiconductor particles becomes smaller than the size (Bohr radius) of the exciton, quantum effects come into play and the particles show an optical behavior that represents an intermediate between that of a bulk semiconductor (featuring energy bands) and that of a semiconductor cluster (with discrete energy levels) (Chapter 1, Figure 1.2) [70, 71]. Quantum effects give rise to band gap widening and hence to a blue shift of the semiconductor absorption edge [72].

Triggered by the search for visible-light driven particle-based photocatalysts, many efforts have been made to develop chemically-modified semiconductor oxides, mainly TiO_2 -based, particle powders, and films absorbing in the visible range [69]. In this context, doping of the semiconductor with metal ions or semiconductor modification by introducing nonmetallic elements such as carbon, nitrogen, and sulfur have been pursued. Though chemical nature and abundance of the impurity species is usually uncontrollable and difficult to assess, UV/Vis spectroscopy has been established as a valuable analytical method for studying electronic transitions involving the respective impurity levels in these materials (Figure 12.14).

12.3.1.3 Excitonic Surface States in Highly Dispersed Insulating Metal Oxides

Discrete bands at energies below the band-to-band transition threshold can be observed on highly dispersed insulating metal oxide particles which are frequently used in heterogeneous catalysis as catalytically active materials or catalyst supports. These excitonic transitions involve low-coordinated surface states, which in the case of alkaline earth oxides are considered to be

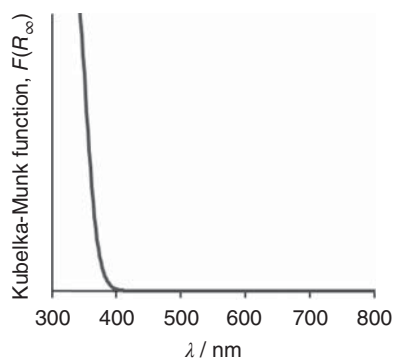
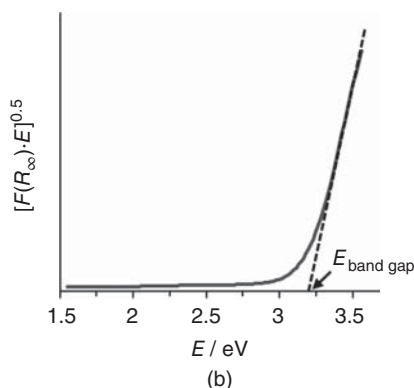


Figure 12.14 (a) Diffuse reflectance spectrum of an anatase TiO_2 nanoparticle powder. (b) The band gap energy can be estimated from the x-axis intercept, which is obtained when extrapolating of the linear part of the modified Kubelka–Munk function.



chemically reactive in base catalysis. DR UV/Vis and PL spectroscopy have been extensively used to characterize MgO, CaO, SrO, and BaO nanoparticle systems with respect to the nature of UV/Vis-active optical transitions as well as the structure and reactivity of the involved surface sites [8]. In selected cases the observation of different bands associated with surface ions of different local coordination has helped to elucidate site-specific physical [73] and/or chemical processes [74–76] on highly dispersed alkaline earth oxides (see Section 12.4.2).

12.3.1.4 Organic Ligands and Adsorbates

Saturated hydrocarbons containing only single bonds exhibit $\sigma \rightarrow \sigma^*$ transitions that require higher energies and are not accessible by standard laboratory UV/Vis spectroscopy equipment. Functional groups that absorb light in the UV and visible region are called chromophores. In particular functional groups that contain multiple bonds and heteroatoms, such as C=O, C \equiv N, C=N, or NO₂, undergo $n \rightarrow \pi^*$ and $\pi \rightarrow \pi^*$ transitions detectable with UV absorption extending into the visible region. Molecules with conjugated double bonds exhibit $\pi \rightarrow \pi^*$ transitions that are shifted to longer wavelengths. Conjugation lowers the energy difference between the highest occupied molecular orbital (HOMO) and the lowest unoccupied molecular orbital (LUMO) resulting in a red shift of the absorption maximum and an increase in intensity. Empirical rules (Woodward–Fieser rules) allow for the prediction of band maxima in conjugated systems [68]. Analysis of molecular species adsorbed on the surface of metal oxides is of particular importance in the investigation of functional materials, such as catalysts (see Section 12.4.1) and organic–inorganic hybrids (see Section 12.4.2). UV/Vis spectroscopy investigations of catalysts during or after operation reveal insights into reaction or deactivation mechanisms of important catalytic transformations such as the isomerization and dehydrogenation of alkanes or the transformation of methanol to olefins [77–79].

12.3.2 Visible Region (3.5–1.5 eV)

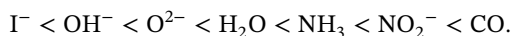
Absorption bands in the visible energy range have been attributed to:

- (i) Metal centered transitions in molecular metal oxide complexes or isolated atoms including
 - $ns \rightarrow np$ in molecular species of main group elements
 - $d \rightarrow d$ or $(n-1)d \rightarrow ns$ in transition metal complexes that contain elements with incompletely filled d^n shells ($1 \leq n \leq 9$)
 - $f \rightarrow f$ or $f \rightarrow d$ in complexes that contain rare earth elements.
- (ii) Collective excitations of conduction electrons in small metal particles with diameters smaller than the wavelength of the incident light (surface plasmon resonance).

12.3.2.1 Metal Centered Transitions

The absorption spectra of metal ions in molecular complexes occurring for example in precursor solutions yield information about nature and oxidation state of the metal ion and its coordination environment. The nonspherical electrostatic field generated by ligands surrounding a central metal atom in a transition metal complex causes energy splitting of the d orbitals with respect to degenerate orbitals in the free metal ion. The splitting is affected by symmetry and geometric arrangement of ligands and Jahn–Teller effects. It is much stronger compared to the splitting caused by electron–electron interactions in free metal ions that contain multiple d electrons. Theoretical description of metal centered transitions is provided by the crystal field theory, which allows interpretation of absorption spectra by treating ions as point charges that undergo pure electrostatic interactions [80]. A more precise analysis of the electronic structure of a coordination compound requires the address of the partial covalent character of metal–ligand bonds. This is implemented in the ligand field theory, which represents a combination of molecular orbital and crystal field theory [81].

Ligands approaching a central atom result in an energy splitting Δ of the d orbitals. For a given coordination number, symmetry, and ligand type, Δ changes little within a period of the periodic table, but increases by moving from top to bottom in a group and with increasing oxidation state of a given element. The nature of the ligand has a strong impact on the extent of splitting. Ligands have been classified according to their order in the spectrochemical series by increasing values of Δ_{oct} in metal complexes with octahedral symmetry. One important example is:



In general, the number of $d \rightarrow d$ transitions depends on the electronic configuration of the molecular coordination compound and the symmetry of the complex. The intensity is generally weak, because $d \rightarrow d$ transitions are Laporte forbidden. Laporte forbidden $(n-1)d \rightarrow ns$, $(n-1)f \rightarrow nd$, and $ns \rightarrow np$ transitions are also observed in the UV/Vis region.

12.3.2.2 Localized Surface Plasmon Resonance

The red color of colloidal metallic gold particles is caused by localized surface plasmon resonance (LSPR). The effect is associated with the size of metal particles in the nanometer range. The decrease in size below the electron mean free path, which is the distance the electron travels between scattering collisions with the lattice atoms in metals, causes intense absorption in the near-UV/Vis [82]. When small metal particles are illuminated with electromagnetic radiation of a wavelength larger than the particle diameter, collective oscillations of conduction electrons (plasmons) are excited [83]. Many metals show more or less distinct absorption in the visible range [84]. The resonance condition for the plasmon depends on particle size, shape, composition,

formation of core-shell structures, or the dielectric constant of the medium [85]. Since the resonance condition can be modulated by synthetic means, plasmonic nanoparticles have been applied in catalysis and photochemistry [86]. The sensitivity of the plasmon resonance depends on the polarity of the solvent leading to the development of biosensors [87]. Plasmon resonance observed on semiconducting metal oxides will be discussed in Section 12.3.3.

The absorption spectra in the UV/Vis are used to characterize metal nanoparticles. The optical properties of larger nanoparticles can be treated theoretically by applying classical electrodynamics including numerical simulation methods, such as Mie theory, discrete dipole approximation (DDA), or the finite difference time domain method [83]. For very small nanoparticles (5–10 nm) where the quantum mechanical effects become important, *ab initio* methods, such as time-dependent density functional theory (TD-DFT), have been employed [88].

12.3.3 Near-Infrared Region (1.5–0.5 μm)

The near-infrared contains metal-centered transitions extending beyond the visible region (3.5–1.5 eV). Furthermore, in NIR

- (i) intraband transitions,
- (ii) vibrational transitions, and
- (iii) localized surface plasmon resonance in semiconductor nanocrystals

are observed.

12.3.3.1 Intraband Transitions: Free Carrier Absorption

In addition to the fundamental band-to-band transition generally observed in the UV range, optical absorption in semiconductors can also take place via indirect transitions within the same energy band (intraband transitions) [89, 90]. This absorption requires the presence of charge carriers, which are free to move inside a band (e.g. electrons in the conduction band) and may, therefore, interact with the ambient. Free carrier absorption is observed in the infrared region of the electromagnetic spectrum and is characterized by a monotonic, structureless spectrum, which grows as λ^p , where p is the scattering constant and λ the photon wavelength. The quantum theory of free carrier absorption is based on the same considerations as the theory of the fundamental absorption in an indirect band gap material (see Section 12.3.1, band-to-band transitions). For momentum conservation, a momentum scattering process is required in addition to the photon absorption. The change in momentum is provided by interaction of the electron with lattice phonons. The scattering constant p can range from 1.5 to 3.5, depending on the statistical weight of the electron scattering mechanisms. The spectral signature of free conduction band electrons has been reported for different semiconductor oxide particle systems such as UV light excited TiO_2 -based powder [91, 92] and H-atom n-doped TiO_2 [54, 93] and ZnO materials [94].

12.3.3.2 Vibrational Transitions

In the near-infrared region additional information such as the combination and overtones of stretching and bending vibrations is accessible. This allows for the simultaneous characterization of organic ligands in metal complexes or adsorbates on metal oxide surfaces and the electronic structure of the central atom or the solid.

Frequently, the coordination of surface metal ions changes when adsorbed molecular water is removed. The structure of water clusters and the presence of hydroxyl groups can be studied in the NIR region. Absorption at around 1950 nm can be assigned to the combination ($\nu_2 + \nu_3$) band of the

bending (ν_2) and asymmetric stretching (ν_3) of the fundamental vibration modes of H_2O . A peak at 1450 nm corresponds to the combination ($\nu_1 + \nu_3$) band of the symmetric (ν_1) and asymmetric (ν_3) stretching vibration modes of water [95]. Furthermore, a peak at 2200 nm was attributed to the combination ($\nu + \delta$) band of the stretching (ν) and bending (δ) modes of silanol groups and a peak at 1380 nm was assigned to the overtone (2ν) absorption band of the stretching (ν) of silanol groups.

12.3.3.3 Localized Surface Plasmon Resonance in Degenerately Doped Metal Oxide Semiconductor Nanocrystals

Some degenerately doped metal oxide semiconductors are capable of supporting localized surface plasmon resonance (LSPR) when synthesized as colloidal nanocrystals. The LSPR originates from collective oscillations of free electrons in the conduction band and can be tuned across the infrared and visible spectrum by varying the nanocrystal size, shape, composition and Fermi level as shown for tin-doped indium oxide (ITO), aluminum-doped zinc oxide (AZO), niobium-doped TiO_2 and other colloidal semiconductor nanocrystals [1, 96]. Such materials are referred to as plasmonic transparent conductive oxides for application in electrochromic devices [1].

12.4 Case Studies

12.4.1 Heterogeneous Catalysis

Metal oxides represent an important class of heterogeneous catalysts used, for example, in acid–base reactions, such as cracking and isomerization, in oxidation of hydrocarbons for synthesis of monomers as a basis for polymerization, such as formaldehyde, acrolein, acrylonitrile, acrylic acid, or maleic anhydride synthesis, in polymerization and metathesis of olefins, in exhaust gas treatments, and in electrodes for electrocatalytic applications and batteries. Developing new, active, selective, and stable catalyst systems requires rational approaches that must be based on a detailed understanding of the surface structures and their transformation under working conditions, as well as knowledge about adsorption and activation of the reacting molecules and the regeneration mechanism of the active sites. Catalytic processes on oxide surfaces generally involve considerable surface dynamics that require structural flexibility of the oxide to guarantee stable operation.

UV/Vis/NIR spectroscopy is a widely-used technique to investigate synthesis [97–100] and dynamics [8, 101–107] of metal oxides applied in heterogeneous catalysis (Figure 12.15). In most of these studies either the electronic properties of a solid, the coordination sphere of a metal center, or redox properties are analyzed. To examine the response of the probed material's properties to the chemical potential of the reaction environment [5, 6, 49, 108–115] or charge transfer steps at electrode interfaces [52, 53, 116], the spectroscopic measurements must be performed during operation of the catalyst [117, 118]. UV/Vis/NIR spectroscopy allows to track degradation processes or to study the interaction of oxides with organic molecules to learn about reaction intermediates or about the mechanism of catalyst deactivation [119–123]. In the following, value and challenges of the method and the importance of integration with complementary techniques and theory will be discussed with reference to some examples.

UV/Vis/NIR spectroscopy is generally performed in combination with other techniques, such as NMR and EPR (Chapter 14), X-ray absorption (Chapter 11), and Raman spectroscopy (Chapter 13), to confirm assignments that are frequently based on phenomenological comparison with spectra of reference compounds. Likewise, multi-method approaches serve as a test to experimentally

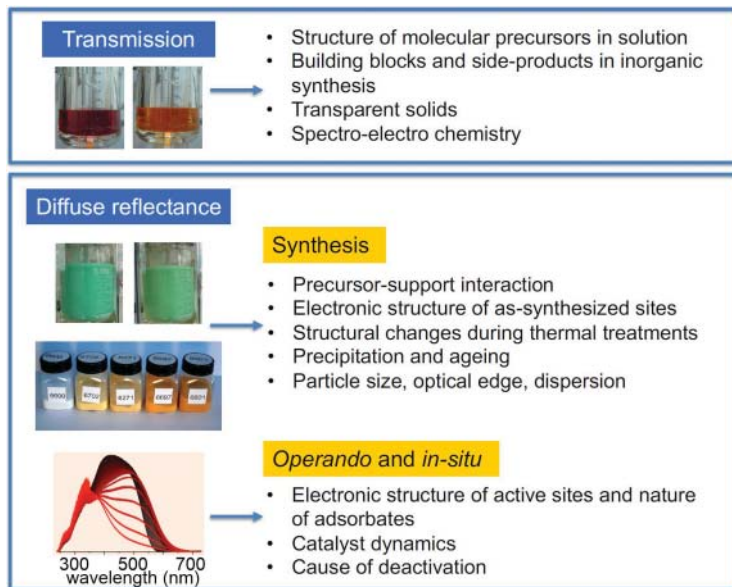


Figure 12.15 Application of UV/Vis/NIR spectroscopy in catalysis.

verify the sensitivity of various spectroscopic techniques with regard to structural differences. Surface sites responsible for high activity and selectivity often represent only a small percentage of the total number of surface sites. The relevant fraction of the active surface (defects, impurities) is often hardly detectable in presence of a majority of chemically and structurally similar spectator species or the species of the matrix in which the active site is embedded. Dehydrated molybdenum oxide supported on mesoporous silica SBA-15 ($\text{MoO}_x/\text{SBA-15}$) is an example that illustrates the difficulty of the task. The material is applied as catalyst in metathesis and oxidation reactions [124]. Molybdenum oxide species anchored on the surface of silica form thin, two-dimensional films that cover the surface to the point where the monolayer is completed. Crystallization of segregated molybdenum oxide nanoparticles generally indicates that the limit of monolayer coverage is exceeded. Catalysts with loadings varying between 2.1 and 13.3 wt% MoO_3 , which corresponds to Mo surface densities between 0.2 and 2.5 Mo atoms nm^{-2} , exhibited very similar spectroscopic fingerprints of UV/Vis and X-ray absorption spectroscopy at the Mo K-edge (for the spectroscopic data see top row of Figure 12.16). Little change in the connectivity of surface molybdenum oxide species or in the coordination geometry of the central Mo atom with increasing molybdenum oxide loading was confirmed by Fourier-transformed Mo K-edge extended X-ray absorption fine structure (EXAFS). UV/Vis spectroscopy in combination with the complimentary X-ray absorption techniques revealed that isolated di-oxo $(\text{Si-O})_2\text{Mo}(=\text{O})_2$ moieties with Mo in tetrahedral coordination are the predominating surface species at all loadings (see cartoons in Figure 12.16). Although all catalysts included in the study were practically indistinguishable by the mentioned spectroscopic techniques, varying functional properties were observed. Enhanced reducibility with increasing Mo oxide loading was measured by temperature-programmed reduction. A maximum in catalytic activity at a coverage close to the completion of the surface monolayer was unisonously found in two very different catalytic reactions. The oxidative dehydrogenation of propane to propylene was performed at high temperature (773K) in presence of oxygen. Propylene metathesis to butene and ethylene was executed at low temperature (323 K) in a reducing atmosphere. The changes in the

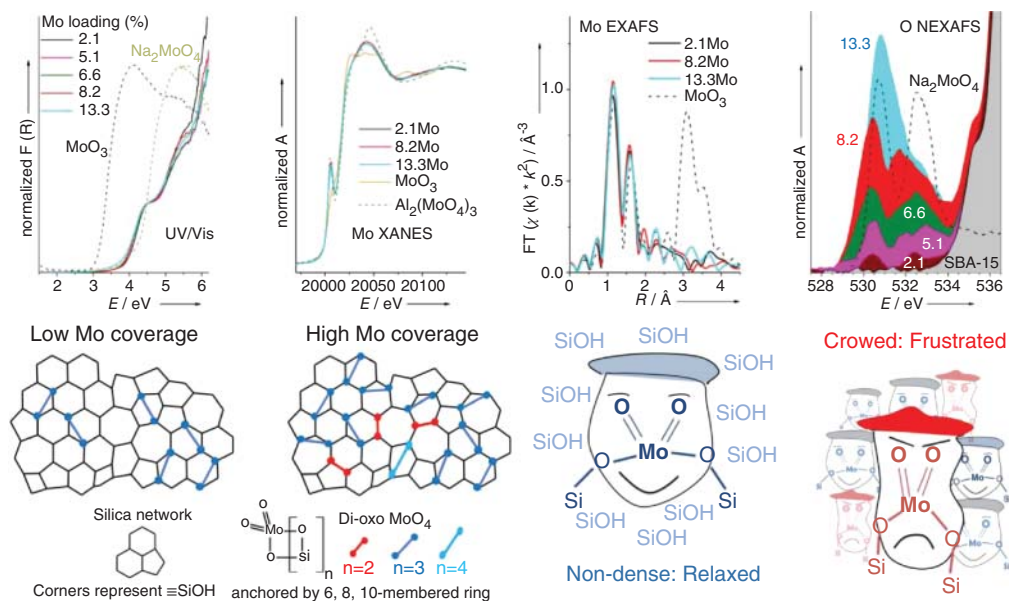


Figure 12.16 UV/Vis, Mo-XANES, Mo-EXAFS, and O-NEXAFS spectra of silica-supported molybdenum oxide catalysts with different Mo loading as indicated in the legends of the spectra shown in the top row. In the bottom row, the formation of isolated di-oxo $(\text{Si}-\text{O}-)_{2}\text{Mo}(=\text{O})_{2}$ moieties during catalyst preparation is illustrated; amorphous silica composed of differently sized siloxane rings is terminated by surface $\text{Si}-\text{OH}$ groups at which the molybdenum oxide species are anchored. At low coverage (blue), energetically equilibrated surface species are formed; at high coverage, some of the sites are strained (red) due to the lack of $\text{Si}-\text{OH}$ groups in suitable distance. Source: Adapted from Amakawa, K., Sun, L., Guo, C. et al. (2013). How strain affects the reactivity of surface metal oxide catalysts. *Angewandte Chemie, International Edition* 52 (51): 13553–13557 [124].

functional properties were only reflected in the near-edge X-ray absorption fine structure (NEXAFS) analysis at the oxygen K-edge (see right figure in the top row of Figure 12.16). According to DFT calculations, the trends in the spectra result from deviations in the bond angles within the di-oxo $(\text{Si}-\text{O}-)_{2}\text{Mo}(=\text{O})_{2}$ species. The Mo–Si distance varies with increasing loading (see bottom row of Figure 12.16), because energetical stable configurations are formed only at low and medium molybdenum oxide loadings. The shortage of suitable anchor sites at high loading leads to the formation of a few strained (frustrated) species that represent only about 1% of the total molybdenum oxide surface sites (see cartoons in Figure 12.16 for illustration). These “high energy sites” might be responsible for the increased catalytic activity of supported molybdenum oxide catalysts with a loading close to the completion of a monolayer.

The example emphasizes the strength of theory in simulating and assigning spectroscopic features [66, 125–127]. Combined experimental and theoretical protocols have been successfully applied in inorganic chemistry and catalysis to elucidate the unknown molecular and electronic surface structure of catalysts. However, model selection and the applied theoretical method have substantial impact on the results obtained by theory. Deviations between experiment and theory originate from oversimplification of the model and methodical errors in calculations, but also from experimental errors and falsifications as outlined in Section 12.2.2.3. Structurally well-defined model systems, such as molecular complexes [66], or crystalline solids [126, 128] can be used to calibrate calculation methods. Successful correlations between experiment and theory reveal not only structural details, but also provide insight into the electronic structure of the system, which is

important to understand the activation of reacting molecules on the surface and the performance of the catalyst. Frequently, however, UV/Vis spectra of surface species are assigned based on comparison with spectra of reference compounds. For example, the phenomenological observation that the optical absorption edge energy decreases with increasing transition metal oxide loading on the surface of various supports suggested that the energy difference between the highest occupied molecular orbital (HOMO) and the lowest unoccupied molecular orbital (LUMO) of the surface complex decreases as the surface density increases. The decrease in HOMO–LUMO energy distance was attributed to an increase in the size of the supported two-dimensional oxide (V, Mo, W, Nb) domains (increase in the degree of oligomerization of supported transition metal oxide species) [129–131]. However, structural changes other than domain size or chain length, such as a modification in the coordination number of the transition metal ion or the type of the ligand, may also occur with increasing loading. These changes might likewise be reflected in the electronic structure, i.e. in the HOMO–LUMO energy difference, and hence in the optical edge energy.

For example, based on *ab initio* calculations, a shoulder at wavelengths longer than 220 nm in the UV/Vis spectrum of single-site titanium ions anchored to the walls of mesoporous silica MCM-41 and MCM-48 was attributed to the presence of OH groups in the coordination sphere of Ti suggesting the existence of $[(\text{OH})\text{Ti}(\text{OSi})_3]$ instead of $[\text{Ti}(\text{OSi})_4]$ Ti(IV) sites [132]. In agreement with this assignment the band disappears after silylation of the material, which converted surface OH groups Ti–OH and Si–OH into $\text{Ti–OSi}(\text{CH}_3)_3$ and $\text{Si–OSi}(\text{CH}_3)_3$, respectively.

Similarly, OH in the coordination sphere of vanadium in V_xO_y surface species supported on mesoporous silica caused a red shift of the absorption edge energy as simulated for the model $(\text{SiO})_2\text{V}(=\text{O})(\text{OH})$ compared to $(\text{SiO})_3\text{V}(=\text{O})$ anchored to a $\text{Si}_8\text{O}_{12}\text{H}_8$ cluster molecule that represents the silica support [126]. The red shift due to the exchange of an O^{2-} ligand by an OH^- ligand is in agreement with the spectrochemical series (Section 12.3.2). The presence of V–OH groups in silica-supported vanadium oxide sub-monolayer catalysts and an increasing amount of V–OH with increasing vanadia loading has been experimentally verified by infrared spectroscopy [133].

Single $(\text{SiO})_3\text{V}=\text{O}$ sites are expected to be the only surface species on the surface of silica-supported vanadium oxide catalysts with low loadings as supposed based on the comparison with optical spectra of reference compounds [131]. However, the combination of several spectroscopic techniques and quantum chemistry revealed that even at very low vanadium oxide loadings on silica (2.3 wt% or 0.6 V atoms nm^{-2} , respectively) a mixture of vanadium oxide species with variable nuclearity exists [66]. The catalyst was investigated in parallel by UV/Vis spectroscopy, V $L_{2,3}$ -edge and O K-edge X-ray absorption spectroscopy, as well as resonance Raman (rR) spectroscopy. Restricted open shell configuration interaction with singles (ROCIS) theory together with time-dependent theory of electronic spectroscopy was applied to calculate XAS, rR, and optical spectra using the ORCA suite of programs (Figure 12.17) [134]. Combined analysis of V $L_{2,3}$ -edge, O K-edge and rR spectra resulted in a distribution involving 5% monomeric, 5% dimeric, 80% trimeric, and 10% tetrameric structures (Case B in Figure 12.17), but other mixtures of oligomers are likewise possible (for example Case A in Figure 12.17). In contrast, a predominant monomeric nature of the surface species is rather unlikely (Case D in Figure 12.17). The example demonstrates that the calculation of a set of spectroscopic observables and their comparison with the corresponding experimental data provides an excellent tool for establishing structure–spectra relationships and to explore the real surface configuration of metal oxide sites. Although time-consuming, it is worthwhile to adopt the technique systematically and to use it also for interpretation of spectra recorded under operation conditions of a catalyst.

The nature of metal oxide species on the surface of heterogeneous catalysts is modified in contact with the reacting medium. Ligand exchange or an extension of the coordination sphere occur

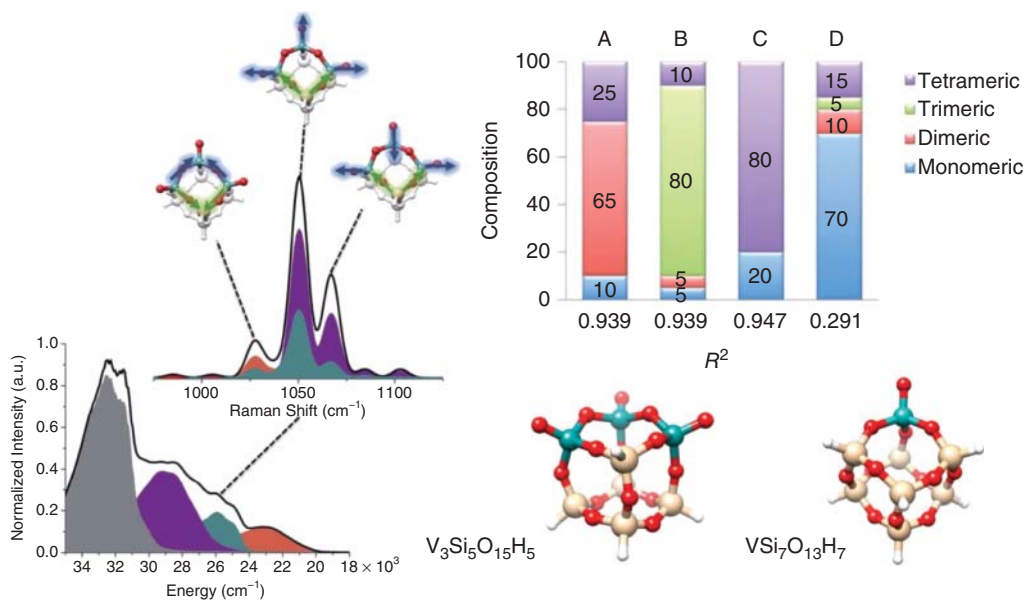


Figure 12.17 Calculated absorption spectra accounting for the band shape of the dominating states for the model $V_3Si_5O_{15}H_5$ (bottom). The states are grouped according to the character of the dominating single-electron excitations involving either $V=O$ and $V-O-V$ sequences (orange), or $V=O$ and $Si-O-V$ sequences (cyan and purple). Raman spectra (left, top) are calculated at an absorption energy of $26\,000\text{ cm}^{-1}$; orange, cyan, and purple bands indicate active vibrational modes pointed with arrows. The simultaneous fit of the weighted superposition of all calculated spectra to the $V\ L_3$ -edge experimental spectrum of 2% V_xO_y/SiO_2 results in different distributions of surface V_xO_y species (top, right). Cases (A), (B), and (C) represent local minima of the fit function corresponding to the best R^2 values achievable by starting the fit either from a pure vanadium oxide dimer, trimer, tetramer, or monomer structure, respectively. The models of the trimer, which is the most abundant (80%) species in Case B, and the monomer (dominating species in Case D) are shown on the right at the bottom. Source: Adapted from Maganas, D., Trunschke, A., Schlögl, R., and Neese, F. (2016). A unified view on heterogeneous and homogeneous catalysts through a combination of spectroscopy and quantum chemistry. *Faraday Discussions* 188: 181–197 [66] RSC.

due to adsorption of the reacting molecule, which is a necessary requirement for the activation of chemical bonds in the molecule on the catalyst surface. Likewise, the adsorption of side and consecutive products can happen. The oxidation state of transition metal ions responds to the redox properties of the reaction mixture. Intermediates and deposits not in contact with the active site, but accumulated on the surface of the support or a binder, may change the optical properties of a working catalyst as well. UV/Vis spectroscopy contributes to an improved understanding of the function of catalysts or their deactivation when performed in the presence of the reacting gas at reaction temperature.

It is distinguished between *operando* and *in situ* spectroscopy. In *in situ* experiments, the reaction conditions are simulated in the spectroscopic cell. In contrast, *operando* spectroscopy implies the *simultaneous* measurement of spectroscopic and catalytic data in one experiment [49]. This is important, because fluid dynamics and temperature distribution inside an *in situ* or *operando* cell are not necessarily the same like in a catalytic test reactor with consequences on gas phase composition, surface coverage, and eventually the electronic and structural properties of the solid and adsorbed species observed by spectroscopy. Therefore, reliable conclusions require *operando* experiments in which spectroscopic and functional properties are measured at the same time. It should

be mentioned at this point that *in situ* experiments, which were performed at relevant reaction temperature and in the presence of realistic gas mixtures, but without evidence of catalytic activity, are sometimes called “*operando*” or a clear statement is missing how and where the catalytic data were measured, which were correlated with spectroscopic features. Such an inconsistent usage of the terminology provokes misleading interpretations.

Operando and *in situ* experiments are predominantly performed either in cells constructed for mirror optics or in reactors equipped with ports to introduce fiber probes. Exceptions are spectro-electrochemical studies of electrodes applied in water splitting for the investigation of the oxygen evolution reaction (OER) [52, 53], or CO₂ activation [116], which are performed in transmission when the electrode material is transparent.

In analogy to the investigation of freshly activated or used catalysts studied *ex situ*, the determination of oxidation states of transition metal ions and coordination geometries of active complexes are major research questions in *in situ* and *operando* studies under working conditions as well. For example, the structure of chromium oxide species in supported CrO_x/SiO₂ catalysts for ethylene polymerization was investigated by a combination of *in situ* and in part *operando* spectroscopic techniques (Raman, UV/Vis, XAS, DRIFTS, and TPSR) [115], Ligand-to-metal charge transfer (LMCT) bands at 250, 340, and 460 nm in the dehydrated catalyst were attributed to isolated surface Cr⁺⁶O_x sites. Under reaction conditions, the initial surface Cr⁺⁶O_x sites are reduced to Cr⁺³ sites as evidenced by the appearance of weak d–d transition bands at 425 and 587 nm forming Cr–(CH₂)₂CH=CH₂ and Cr–CH=CH₂ reaction intermediates. The evolution of the surface Cr⁺³–CH=CH₂ reaction intermediate correlates with the formation of the polyethylene product suggesting that the species are the active reaction intermediates.

In addition to the characterization of electronic properties of transition metal sites, *operando* and *in situ* UV/Vis spectroscopy has been applied to monitor the deposition of carbonaceous species on the surface of catalysts for example in the dehydrogenation of alkanes to olefins [119], the isomerization of alkanes [77], and methanol to olefin or gasoline processes over zeolites [120].

The methanol-to-hydrocarbons (MTH) process is a potential, technically proven route from alternative carbon sources, such as coal, natural gas, biomass, and CO₂, to chemicals and fuels. The process consists in the production of synthesis gas, a mixture of hydrogen, carbon monoxide and carbon dioxide, the transformation of synthesis gas to methanol over a Cu/ZnO/Al₂O₃ catalyst and finally the formation of gasoline-rich (methanol to gasoline; MTG) or olefin-rich (methanol to olefins; MTO) product mixtures depending on the nature of catalyst and reaction conditions. The catalyst of the latter process is a crystalline, microporous aluminosilicate, such as ZSM-5, or a silicoaluminophosphate, such as SAPO-34. Product formation in the final step takes place over hybrid organic (hydrocarbon pool)–inorganic sites, the composition of which depends on zeolite topology [121]. UV/Vis spectroscopy contributes to an understanding of mechanistic aspects and catalyst deactivation [122, 123]. In a combined *operando* X-ray diffraction and UV/Vis study (Figure 12.18) it was shown that the formation of the hydrocarbon pool in small-pore zeolite catalysts, where the size of the pores is limited by eight-ring windows, causes the zeolite lattice to expand and the catalyst to deactivate [135]. The nature of the retained hydrocarbons was simultaneously determined by *operando* UV/Vis spectroscopy. A catalyst with CHA framework exhibited 0.9% expansion in the direction along the *c*-axis of the zeolite lattice caused by formation of methylated naphthalene and pyrene. The experimental setup, which was used in the *operando* experiment, is shown together with the results in Figure 12.18.

In summary, UV/Vis/NIR spectroscopy is an important method applied in synthesis and functional characterization of heterogeneous catalysts. During synthesis, the chemical nature of molecular precursors and the properties of reaction intermediates and products are analyzed. Fresh and

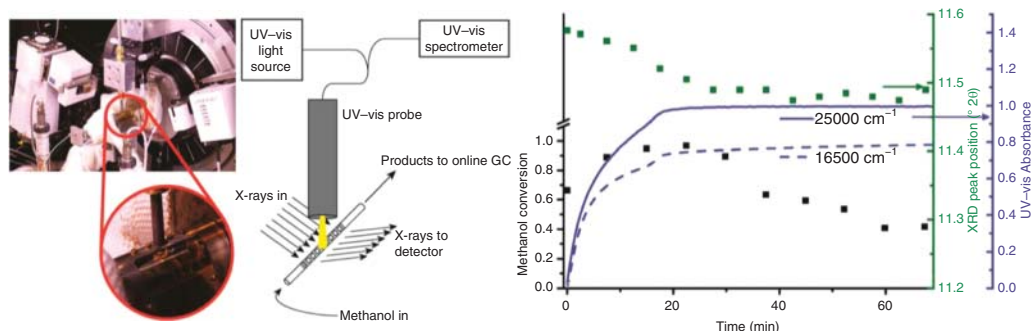


Figure 12.18 Schematic illustration of a combined *operando* X-ray diffraction and UV/Vis setup (left) that was used to measure the relation between methanol conversion (activation followed by deactivation after 20 minutes time on stream, lower squares), lattice expansion (XRD peak position, upper squares), and amount of deposited hydrocarbon species (UV/Vis absorbance at 25 000 and 16 500 cm^{-1} , solid and dotted lines, respectively) in the cages of a small-pore zeolite with CHA structure (right). Source: Adapted from Goetze, J., Yarulina, I., Gascon, J. et al. (2018). Revealing lattice expansion of small-pore zeolite catalysts during the methanol-to-olefins process using combined *operando* X-ray diffraction and UV-vis spectroscopy. *ACS Catalysis* 8 (3): 2060–2070 [135]. © 2018, American Chemical Society.

spent catalysts as well as working catalysts are investigated with regard to electronic bulk properties and defects, and the coordination sphere or oxidation state of metal centers. In addition, adsorption of reacting molecules and intermediates and the formation of deposits that potentially lead to catalyst deactivation are studied. Application of complementary spectroscopic techniques and theory is required to cope with the detection of minority species in presence of chemically and structurally similar spectator species, to attain reliable assignments of spectroscopic features, and to gain insight into the electronic structure of the catalysts and surface species. The knowledge is important to understand the activation of reacting molecules on gas–solid or liquid–solid interfaces and the dynamic response of the catalyst to thermodynamic and chemical parameters of the reaction environment.

12.4.2 Adsorption and Reaction of Porphyrins on Highly Dispersed MgO Nanocube Powders

The functionalization of nanostructured metal oxides with organic molecules and the implementation of resulting organic–inorganic hybrids into devices [18, 136] requires detailed knowledge about the reactivity and the stability of the organic–inorganic interfaces in different chemical environments. Microscopic-level insight into the interface between the organic molecule and the oxide material and into interfacial electron and proton transfer processes is particularly important for emerging applications in solar energy conversion, photocatalytic reactors, electrochromic devices, or new materials for sensing and rewritable storage media [137, 138].

High quantum yields of light-driven charge separation can be achieved at dye/semiconductor oxide interfaces. This is exploited in dye-sensitized solar cells (DSSCs) to convert light into electrical energy (regenerative DSSC) or in chemical fuels (photosynthetic DSSC) [139, 140]. The photoanodes used in these photoelectrochemical cells (Figure 12.19) consist of semiconductor oxide electrodes (e.g. anatase TiO_2 nanoparticle films) with high surface area. Adsorbed dye molecules harvest a large fraction of the incident solar light. Porphyrins have received attention as promising photosensitizers because of the broad variety of synthetic modification possibilities through which their physicochemical properties can be tuned on the molecular level [141, 142].

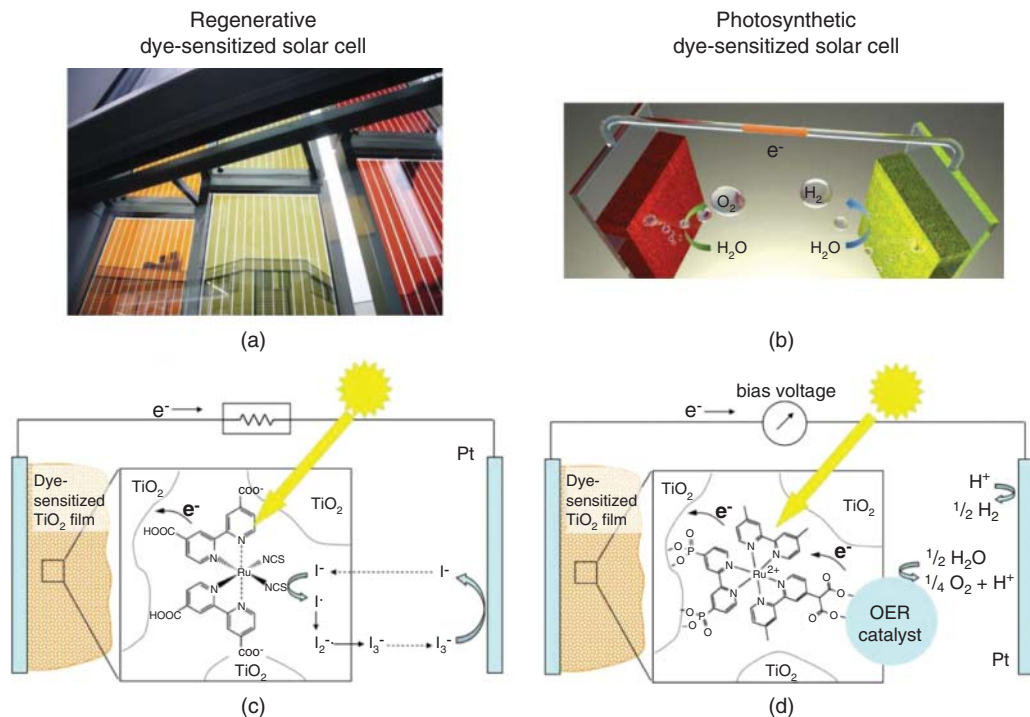


Figure 12.19 (a) Regenerative and (b) photosynthetic dye-sensitized solar cells (DSSCs) and schematic illustrations of the working principles (c, d). In regenerative DSSCs (a, c) light is converted into electric energy while the anode and cathode reactions are the reverse of each other (involving a redox shuttle such as the frequently used iodide/triiodide redox pair). In photosynthetic DSSCs for water splitting (b, d) oxygen is evolved at the dye-sensitized photoanode and water is reduced to hydrogen at a dark catalytic cathode. A catalyst for the oxygen evolution reaction (OER) is bound to or co-adsorbed with the sensitizer on the photoanode. Typically a small cathodic bias is needed to drive this reaction. Source: Adapted with permission from Xu, P., McCool, N.S., and Mallouk, T.E. (2017). Water splitting dye-sensitized solar cells. *Nano Today* 14: 42–58 [140]; and Barraud, E. (2013). Stained glass solar windows for the swiss tech convention center. *Chimia* 67 (3): 181–182 [143].

One important factor determining the performance of DSSCs is the ability of the photoexcited dye to inject an electron into the conduction band of the semiconductor (Figure 12.19). The optoelectronic properties of the photoanode depend on the properties of both the semiconductor and the dye as well as on the mode of dye attachment to the metal oxide surface and on the orientation of the dye molecules at the interface [144–146]. A monolayer of homogeneously spaced dyes is desirable to assure an efficient charge injection from the dye to the semiconductor as well as an efficient dye regeneration. The aggregation of dye molecules at the interface can hamper such an ideal situation and negatively affect device performance. The nature and extent of dye aggregation at the surface of metal oxide nanocrystals therefore needs to be understood in detail if its effect on photovoltaic function is to be discerned [145].

Although the chemical understanding of porphyrin adsorption and the knowledge on coverages and adsorbate geometries on metal oxide particle systems are an important prerequisite to enhance the performance of these hybrid materials, there is still a lack of qualitative and quantitative information on porphyrin binding and associated surface chemistry. This lacuna can be attributed to the immanent structural and compositional complexity of metal oxide nanoparticle-based hybrid systems. However, lowering and controlling this complexity can be an effective strategy

for gaining microscopic-level insight into interfacial processes taking place in these systems. Towards this aim, tailored and well-defined model particle systems with interface properties that are straightforwardly accessible to experiment are indispensable [147].

The following section aims at highlighting the possibilities of using molecular spectroscopies, with particular reference given to DR-UV/Vis and PL spectroscopies, for gaining qualitative and quantitative information on porphyrin adsorption and reactivity on the surface of morphologically well-defined MgO nanoparticle systems [76, 148, 149], which have been established as model systems for adsorption studies on metal oxide particle systems.

MgO nanocube powders were obtained by chemical vapor synthesis (CVS) [150] and are well-defined in terms of morphology featuring isolated primary particles of cubic shape [151]. After synthesis these particle powders were annealed in high vacuum as well as in pure oxygen atmosphere in order to eliminate surface contaminants that may affect the adsorption process. The activated MgO nanocubes are characterized by a narrow particle size distribution below 10 nm with an average edge length of about 6 nm (Figure 12.20).

Comparative adsorption studies were performed using different porphyrin derivatives (Figure 12.20), some of them featuring carboxyl groups on each of the four phenyl rings (5,10,15,20-tetrakis(4-carboxyphenyl)-21,23H-porphyrin; 2HTCPP) and some of them not (5,10,15,20-tetraphenyl-21,23H-porphyrin; 2HTPP). The vapor phase grown MgO nanocube powder (400 mg) was contacted with solutions (25 mL) of 2HTPP in toluene or 2HTCPP in methanol, respectively [148, 149]. In each case the particles remained in dispersion for approximately 24 h. This treatment does not alter the primary particle properties such as their size and shape.

Contact of a MgO nanocube powder with a 2HTPP solution produces significant optical changes both in the supernatant solution as well as in the powder (Figure 12.21). Starting at low porphyrin concentrations ($c < 1 \times 10^{-3} \text{ mol l}^{-1}$) the color of the initially purple solution (left quartz glass cell in Figure 12.21) fades and a colorless clear solution is obtained (right quartz glass cell in Figure 12.21). At the same time, the originally white MgO powder adopts a dark green color.

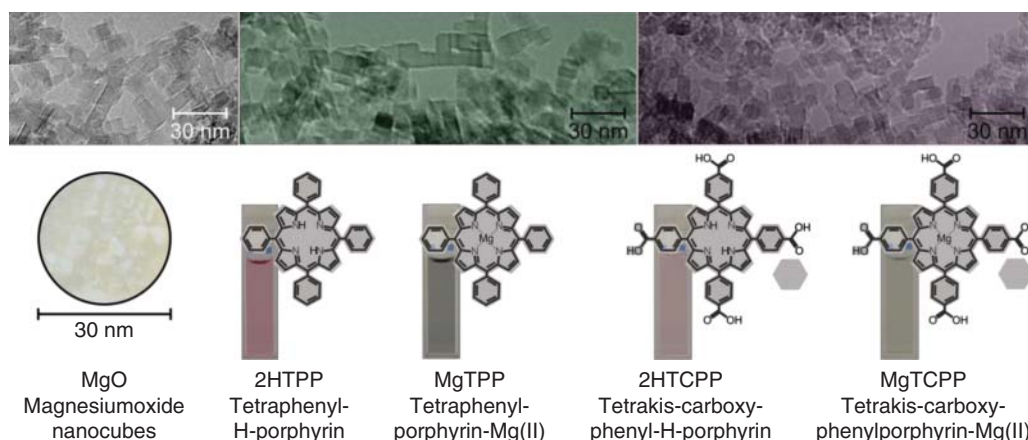


Figure 12.20 MgO nanocube powders (transmission electron microscopy images and digital micrograph) and different porphyrin types in organic solution. The difference in color arises from changes in the metalation state of the porphyrins. Source: Reprinted from Schneider, J., Kollhoff, F., Schindler, T. et al. (2016). Adsorption, ordering, and metalation of porphyrins on MgO nanocube surfaces: The directional role of carboxylic anchoring groups. *Journal of Physical Chemistry C* 120 (47): 26879–26888 [149] ACS publications.

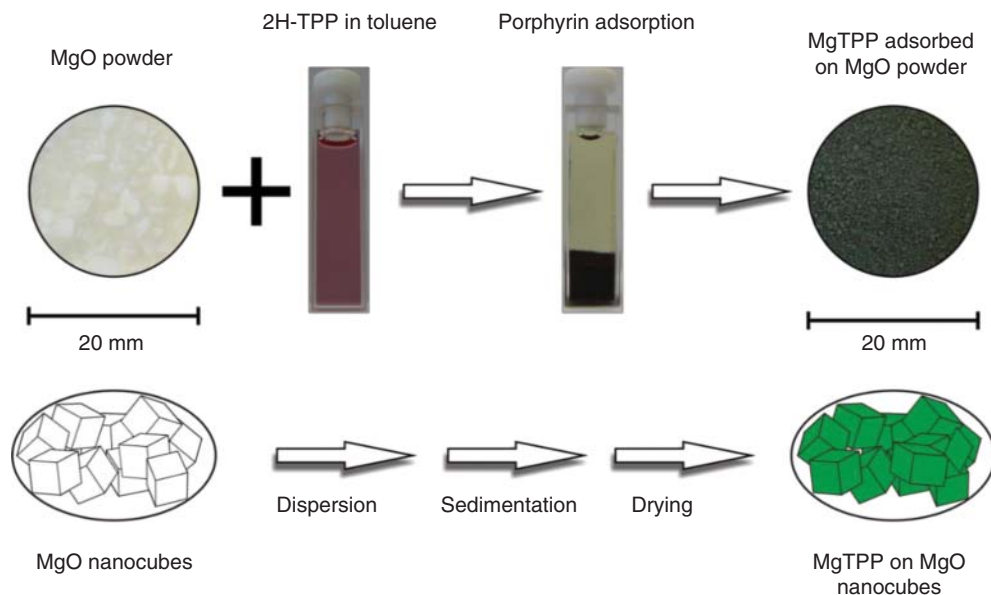


Figure 12.21 Scheme which illustrates the experimental procedure of 2HTPP adsorption at MgO nanocubes which by porphyrin metalation leads to the discoloration of the porphyrin solution and coloration the MgO nanocube powder. Source: Reprinted from Schneider, J., Kollhoff, F., Bernardi, J. et al. (2015). Porphyrin metalation at the MgO nanocube/toluene interface. *ACS Applied Materials and Interfaces* 7 (41): 22962–22969 [148] ACS Publications.

DR-UV/Vis and PL spectroscopies were used to resolve the molecular origin of the optical changes observed in the material (Figure 12.22). The absorption spectrum of porphyrins in the UV/Vis range results from two characteristic contributions: An intense absorption band in the range between $3.1 \text{ eV} > E > 2.5 \text{ eV}$ ($400 \text{ nm} < \lambda < 500 \text{ nm}$, Figure 12.22, left) which is attributed to the B- (or Soret)-band related to the $S_0 \rightarrow S_2(\pi, \pi^*)$ transition [152].

In addition, weaker bands in the range $2.5 \text{ eV} > E > 1.8 \text{ eV}$ ($500 \text{ nm} < \lambda < 700 \text{ nm}$), referred to as Q-bands, are consistent with $S_0 \rightarrow S_1(\pi, \pi^*)$ transitions that are split into different vibrational states (Q(0,0) and Q(0,1)). Whereas the UV/Vis spectra of free-base porphyrins show four Q-bands (Figure 12.22c, left), the higher symmetry of the molecular center in the metalated porphyrin gives rise to a simple spectrum with only two Q-bands (Figure 12.22b, left) [142, 153].

After MgO nanocube dispersion in a 2HTPP solution and subsequent drying, the UV/Vis DR spectrum of the MgO nanocube powder shows an intense Soret-band at 2.92 eV (425 nm) and two additional well-separated bands at 2.19 eV (565 nm) and 2.03 eV (610 nm) (Figure 12.22a, left). Comparison of this spectral region with that of 2HTPP and MgTPP in solution with the above mentioned Q-bands (Figure 12.22b and c, left) provides evidence for adsorptive metalation of porphyrin at the toluene/MgO interface at room temperature.

After contact of the MgO nanocube powder with the porphyrin solution the respective PL emission spectrum reveals two bands at 2.00 eV (620 nm) and at 1.85 eV (670 nm) as well as a minor contribution at 1.72 eV (720 nm) (Figure 12.22a, right). With regard to the energies of the band maxima the two main emission bands are in good agreement with those measured for MgTPP in toluene solution (Figure 12.22b, right). Consistent with UV/Vis DR, photoluminescence provides further evidence for the metalation of the porphyrin at room temperature on the MgO nanocube surface. The third independent spectroscopic evidence for porphyrin metalation was provided by

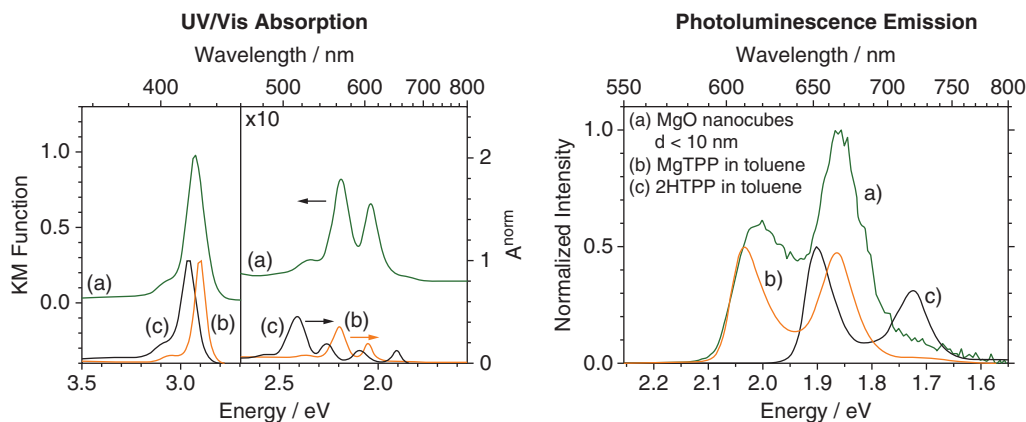


Figure 12.22 UV/Vis spectra (left) and photoluminescence emission spectra (right) of MgTPP adsorbed on MgO nanocubes (a) as well as MgTPP and 2HTPP in toluene (b and c, respectively). The porphyrin was adsorbed on MgO nanocubes from an anhydrous toluene solution with a 2HTPP concentration of 10^{-5} mol L $^{-1}$. Source: Reprinted from Schneider, J., Kollhoff, F., Bernardi, J. et al. (2015). Porphyrin metalation at the MgO nanocube/toluene interface. *ACS Applied Materials and Interfaces* 7 (41): 22962–22969 [148] ACS Publications.

diffuse reflectance infrared Fourier transform spectroscopy (DRIFTS) measurements, which reveal the absence of the asymmetric $\nu_{\text{as}}(\text{N-H})$ stretching vibration characteristic of the free base form of the porphyrin after adsorption on MgO nanocubes [148, 149].

The number of adsorbed and metalated porphyrin molecules per MgO nanocube was photometrically determined using 2HTPP solutions with different initial concentrations (Figure 12.23). In porphyrin solutions with initial concentrations $c < 1 \times 10^{-3}$ mol L $^{-1}$, quantitative adsorption and metalation was observed and demonstrated by the complete discoloration of the supernatant solution (right quartz glass cell of Figure 12.21). At 2HTPP concentrations $c > 5 \times 10^{-3}$ mol L $^{-1}$, the number of adsorbed molecules saturates at a level which corresponds to 80 ± 5 molecules per MgO nanocube, a coverage that corresponds to one monolayer of porphyrin molecules adsorbed in a flat-lying geometry. The vast majority of porphyrin adsorbs on MgO nanocubes in the metalated form. For larger MgO cubes with a size in the range of $10 \text{ nm} \leq d \leq 1000 \text{ nm}$, on the contrary, adsorbed porphyrins exist mainly as the free base. Apparently, only a small fraction of the surface sites are capable of donating Mg^{2+} ions and deprotonating the porphyrin.

In certain cases, morphologically well-defined nanoparticle systems such as MgO nanocube powders may facilitate the transfer of surface science insights and of theoretical models to technologically relevant high surface area materials [76]. Aiming at potential site-specific insights, the adsorption of 2HTPP on MgO nanocube powders was also addressed at the solid–vacuum interface [76]. While high vacuum conditions constitute a quite unrealistic model situation for nanohybrid preparation, they allow however for gaining further insights into the reactive adsorption sites due to the following reasons:

- i) The reduction of the system complexity by the removal of the surrounding condensed phase allows to contrast observations on nanoparticle systems with conclusions drawn from ultrahigh vacuum-grown and atomically clean thin MgO films and with results from density functional theory (DFT) calculations [76].
- ii) For highly dispersed alkaline earth metal oxide powders at high vacuum conditions, DR UV/Vis and PL spectroscopies may be used as surface sensitive analytical methods.

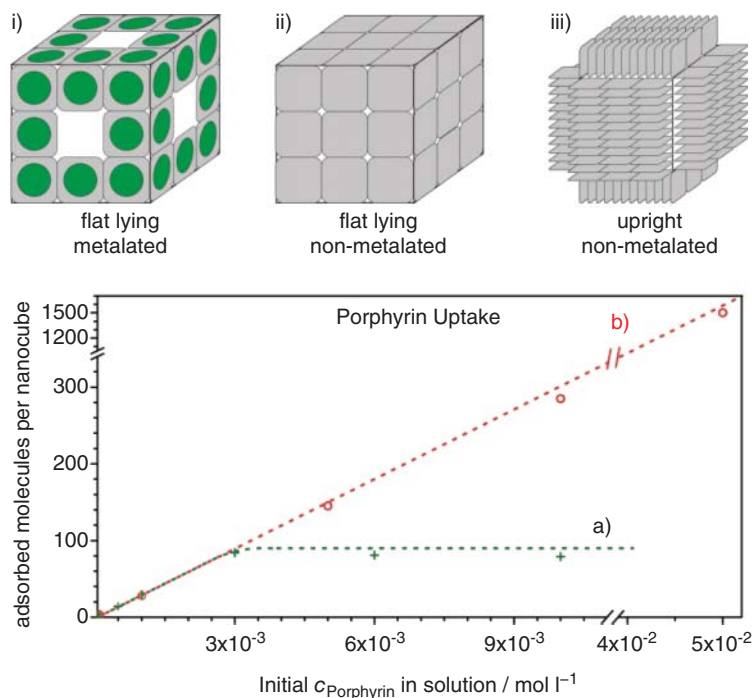


Figure 12.23 Proposed adsorption geometries (i–iii) of non-metalated or metalated 2HTPP and 2HTCPP molecules on the MgO nanocube surface and uptake-curves for 2HTPP (a) and 2HTCPP (b) on MgO nanocubes. For 2HTPP adsorption the coverage saturates at approximately 90 molecules per nanocube. 2HTCPP adsorbs quantitatively in the concentration range up to $c = 5 \times 10^{-2} \text{ mol l}^{-1}$. This concentration corresponds roughly to 1500 molecules per nanocube. Source: Reprinted from Schneider, J., Kollhoff, F., Schindler, T. et al. (2016). Adsorption, ordering, and metalation of porphyrins on MgO nanocube surfaces: The directional role of carboxylic anchoring groups. *Journal of Physical Chemistry C* 120 (47): 26879–26888 [149] ACS Publications.

Low-coordinated sites present on the surface of MgO nanocubes can be identified by DR-UV/Vis spectroscopy by characteristic absorptions in the UV range (Section 12.3.1.3). Absorption features at 5.6 eV (220 nm) and at 4.7 eV (270 nm) result from electronic transitions at edge and corner regions of the MgO nanocubes [154]. Upon porphyrin adsorption, the intensities of these features decrease, which points to the participation of the corresponding sites in the adsorption process.

According to DFT calculations [76] 2HTPP adsorption can be attributed to the presence of low coordinated Mg sites, e.g. corners and edges:



The two protons, which are released by the free-base porphyrin after the uptake of the Mg^{2+} ion, are expected to convert two surface oxygen anions into OH groups [76]. The reaction can be viewed as an ion exchange between the two aminic protons of the 2HTPP molecules with an Mg^{2+} ion from the surface (Eq. (12.10)), where the driving force for the reaction is the high stability of the formed hydroxyl groups along steps and defects on the MgO surface [76]. DFT calculations find MgTPP formation to be strongly exothermic at corners, edges, and steps, but slightly endothermic on terrace sites. This agrees well with UV/Vis diffuse reflectance, which upon adsorption of 2HTPP shows a decrease in the absorption band associated with corner and edge sites on MgO nanocube powders. The results indicate porphyrin metalation at corner and edge sites of MgO and

provide unambiguous evidence for MgTPP adsorption at coordinatively unsaturated sites of the MgO nanocube surfaces.

The limited mobility of MgTPP at the surface of MgO nanocubes is assumed to confine the molecules to the close proximity of those reactive corner or edge sites where porphyrin metalation takes place. Consequently, the process of porphyrin metalation and adsorption would be self-limiting provided that MgTPP desorption into the toluene bulk does not contribute to the recovery of the reactive sites. Indeed, it was observed that the porphyrins – once metalated at the MgO/toluene interface – remain adsorbed even after repeated washing cycles with the pure solvent.

The presence of functional groups (such as carboxylic acid moieties) in the molecular structure of the organic molecules may significantly modify interfacial processes taking place at hybrid materials. To study the impact of carboxylic groups at the periphery of the molecule on the adsorption and reactivity of porphyrins at the surface of MgO nanocubes, the behavior of 2HTPP was contrasted with the behavior of 2HTCPP (Figure 12.20) [149].

After contact with methanolic 2HTCPP solutions, the MgO nanocube powder features an intense dark red color. The corresponding UV/Vis spectra show a good match with the spectrum of non-metalated 2HTCPP in solution. From this observation it can be concluded that – in contrast to 2HTPP – porphyrin adsorption takes place via one or more carboxylate groups in the case of 2HTCPP and a consecutive metalation reaction is suppressed. In strong contrast to 2HTPP adsorption, 2HTCPP is adsorbed quantitatively up to the maximum concentration investigated (Figure 12.23b). This is evident from the complete decoloration of the supernatant solutions for all concentrations studied. The maximum number of adsorbed 2HTCPP molecules can be as high as 1500 molecules per MgO nanocube (Figure 12.23b).

These observations together with results from DRIFTS measurements [149] are in line with an adsorption model where the 2HTCPP molecule binds via one or two carboxyl groups. Those carboxyl groups not linked to the MgO surface would be available for multilayer formation. In that case the density of molecules inside the monolayer would be significantly higher and multilayer formation via interacting carboxyl groups (H-bonds, anhydride formation) would be expected. With regard to the consecutive surface chemistry it was found that 2HTPP molecules metalate at the MgO surface, whereas the 2HTCPP molecules do not. Possibly, surface anchoring via external carboxylic acid groups and steric limitations do suppress the porphyrin molecule center's approach to the nanocube surface and – consequently – the metalation step [76, 148].

The site selectivity of porphyrin adsorption and of a possible consecutive metalation reaction on metal oxide nanostructures is a promising approach for the spatial organization of photo-active molecules in metal oxide hybrid structures. DR UV/Vis and PL spectroscopies have turned out as powerful tools to follow associated interfacial processes qualitatively and quantitatively at a microscopic level.

Nomenclature

a, A, K_λ	Absorption coefficient [cm^{-1}]
A_{10}	Spectral absorbance [-]
c_0	Speed of light ($c_0 = 299\,792\,458\text{ m s}^{-1}$)
c	Concentration of absorbing species [mol cm^{-3}]
ΔE	Energy difference between the initial and the final state of a spectroscopic transition [eV]

$E_{\text{band gap}}$	Band gap energy [eV]
E_{phonon}	Phonon energy [eV]
ϵ	Molar extinction coefficient [$1 \text{ mol}^{-1} \text{ cm}^{-1}$]
$F(R_{\infty})_{\lambda}$	Kubelka–Munk function (remission function) [-]
h	Planck constant ($h = 6.626 \times 10^{-34} \text{ J s} = 4.136 \times 10^{-15} \text{ eV s}$)
I	Intensity (radiation flux) of transmitted light [W m^{-2}]
I_0	Intensity (radiation flux) of incident light [W m^{-2}]
I_{em}	Intensity (radiation flux) of emitted light [$\text{W}\cdot\text{m}^{-2}$]
I_r	Intensity (radiation flux) of reflected light [$\text{W}\cdot\text{m}^{-2}$]
J	Intensity (radiation flux) of diffuse reflected light [$\text{W}\cdot\text{m}^{-2}$]
k_r, k_{nr}	First order rate constants associated with the radiative decay (k_r) and all possible nonradiative decay processes (k_{nr}) of an electronically excited state [s^{-1}]
ℓ	Optical path length [cm]
λ	Wavelength of light [nm]
λ_{exc}	Wavelength of the excitation light [nm]
λ_{em}	Wavelength of the emitted light [nm]
ν	Frequency of light [s^{-1}]
$\tilde{\nu}$	Wavenumber of light [cm^{-1}]
n_p	Refractive index of a particle [-]
n_m	Refractive index of the matrix [-]
r	Radius of spherical scatterers [nm]
R	Reflectance [-]
$\text{Log}(1/R)$	Apparent absorbance [-]
R_{∞}	Diffuse reflectance of an infinitely thick, opaque layer of the sample [-]
R_0	Diffuse reflectance of a sample that either absorbs or transmits all light [-]
S	Scattering coefficient [cm^{-1}]
T, T_{λ}	Transmittance [-]
τ	Lifetime of an electronically excited state [s]
ϕ_p	Volume fraction of metal oxide particles [-]
ϕ	Quantum efficiency of photoluminescence [-]
x	Thickness of the medium [cm]

List of Abbreviations

ATR	attenuated total reflection
AZO	aluminum-doped zinc oxide
CT	charge transfer
CVS	chemical vapor synthesis
DDA	discrete dipole approximation
DFT	density functional theory
DR	diffuse reflectance
DRS	diffuse reflectance spectroscopy
DRIFTS	diffuse reflectance infrared Fourier transform spectroscopy
EPR	electron paramagnetic resonance
EXAFS	extended X-ray absorption fine structure
HOMO	highest occupied molecular orbital
IR	infrared

IRRAS	infrared reflection absorption spectroscopy
ITO	tin-doped indium oxide
LED	light-emitting diode
LMCT	ligand-to-metal charge transfer
LSPR	localized surface plasmon resonance
LUMO	lowest unoccupied molecular orbital
MMCT	metal-to-metal charge transfer
MLCT	metal-to-ligand charge transfer
MTH	methanol to hydrocarbons
MTG	methanol to gasoline
MTO	methanol to olefins
NEXAFS	near-edge X-ray absorption fine structure
NIR	near-infrared
NMR	nuclear magnetic resonance
OER	oxygen evolution reaction
PL	photoluminescence
PMMA	poly (methyl methacrylate)
PTFE	polytetrafluoroethylene
ROCIS	restricted open shell configuration interaction with singles
rR	resonance Raman
SAPO-34	silicoaluminophosphate-34
SBU	secondary building unit
SCR	selective catalytic reduction
TD-DFT	time-dependent density functional theory
TEM	transmission electron microscopy
UV	ultraviolet
Vis	visible
XAS	X-ray absorption spectroscopy
XANES	X-ray absorption near-edge structure
ZSM-5	Zeolite Socony Mobil - 5
2HTPP	5,10,15,20-tetraphenyl-21,23H-porphyrin
2HTCPP	5,10,15,20-tetrakis(4-carboxyphenyl)-21,23H-porphyrin

References

- 1 Runnerstrom, E.L., Llordés, A., Lounis, S.D., and Milliron, D.J. (2014). Nanostructured electrochromic smart windows: Traditional materials and NIR-selective plasmonic nanocrystals. *Chemical Communications* 50 (73): 10555–10572.
- 2 McKittrick, J. and Shea-Rohwer, L.E. (2014). Review: Down conversion materials for solid-state lighting. *Journal of the American Ceramic Society* 97 (5): 1327–1352.
- 3 Althues, H., Henle, J., and Kaskel, S. (2007). Functional inorganic nanofillers for transparent polymers. *Chemical Society Reviews* 36 (9): 1454–1465.
- 4 Calvo, M.E., Castro Smirnov, J.R., and Míguez, H. (2012). Novel approaches to flexible visible transparent hybrid films for ultraviolet protection. *Journal of Polymer Science, Part B: Polymer Physics* 50 (14): 945–956.

- 5 Jentoft, F.C. (2012). Electronic spectroscopy: Ultra violet-visible and near IR spectroscopies: In: *Characterization of Solid Materials and Heterogeneous Catalysts: From Structure to Surface Reactivity, Volume 1 and 2* (M. Che and J.C. Vedrine), 89–147. Weinheim: Wiley-VCH.
- 6 Jentoft, F.C. (2009). Chapter 3 Ultraviolet-visible-near infrared spectroscopy in catalysis. Theory, experiment, analysis, and application under reaction conditions. *Advances in Catalysis, Volume 52*, 129–211. Academic Press.
- 7 Matsuoka, M., Saito, M., and Anpo, M. (2012). Photoluminescence spectroscopy. In: *Characterization of Solid Materials and Heterogeneous Catalysts: From Structure to Surface Reactivity, Volume 1 and 2* (M. Che and J.C. Vedrine), pp. 149–184. Weinheim: Wiley-VCH.
- 8 Martra, G., Gianotti, E., and Coluccia, S. (2009). The Application of UV-visible-NIR spectroscopy to oxides. In: *Metal Oxide Catalysis* (S.D. Jackson and J.S.J. Hargreaves), 51–94. Wiley-VCH.
- 9 Hanemann, T. and Szabó, D.V. (2010). Polymer-nanoparticle composites: From synthesis to modern applications. *Materials* 3 (6): 3468–3517.
- 10 Demir, M.M. and Wegner, G. (2012). Challenges in the preparation of optical polymer composites with nanosized pigment particles: A review on recent efforts. *Macromolecular Materials and Engineering* 297 (9): 838–863.
- 11 Berger, T., Monllor-Satoca, D., Jankulovska, M. et al. (2012). The electrochemistry of nanostructured titanium dioxide electrodes. *ChemPhysChem* 13 (12): 2824–2875.
- 12 Bai, Y., Mora-Seró, I., de Angelis, F. et al. (2014). Titanium dioxide nanomaterials for photovoltaic applications. *Chemical Reviews* 114 (19): 10095–10130.
- 13 Braun, J.H., Baidins, A., and Marganski, R.E. (1992). TiO₂ pigment technology: A review. *Progress in Organic Coatings* 20 (2): 105–138.
- 14 Diebold, M.P. (2014). *Application of Light Scattering to Coatings*. Springer.
- 15 Jiang, S., van Dyk, A., Maurice, A. et al. (2017). Design colloidal particle morphology and self-assembly for coating applications. *Chemical Society Reviews* 46 (12): 3792–3807.
- 16 Prakash, J., Kumar, V., Erasmus, L.J.B. et al. (2018). Phosphor polymer nanocomposite: ZnO:Tb³⁺ embedded polystyrene nanocomposite thin films for solid-state lighting applications. *ACS Applied Nano Materials* 1 (2): 977–988.
- 17 Demir, M.M., Koynov, K., Akbey, Ü. et al. (2007). Optical properties of composites of PMMA and surface-modified zincite nanoparticles. *Macromolecules* 40 (4): 1089–1100.
- 18 Kickelbick, G. (2007). *Hybrid Materials: Synthesis, Characterization, and Applications*. Wiley-VCH.
- 19 Landers, J., Colon-Ortiz, J., Zong, K. et al. (2016). In situ growth and characterization of metal oxide nanoparticles within polyelectrolyte membranes. *Angewandte Chemie, International Edition* 55 (38): 11522–11527.
- 20 Matijević, E. (1993). Preparation and properties of uniform size colloids. *Chemistry of Materials* 5 (4): 412–426.
- 21 Zhang, L., Blom, D.A., and Wang, H. (2011). Au-Cu₂O core-shell nanoparticles: A hybrid metal-semiconductor heteronanostructure with geometrically tunable optical properties. *Chemistry of Materials* 23 (20): 4587–4598.
- 22 Schoonheydt, R.A. (2010). UV-VIS-NIR spectroscopy and microscopy of heterogeneous catalysts. *Chemical Society Reviews* 39 (12): 5051–5066.
- 23 Meunier, F.C. (2010). The design and testing of kinetically-appropriate operando spectroscopic cells for investigating heterogeneous catalytic reactions. *Chemical Society Reviews* 39 (12): 4602–4614.

- 24 Andanson, J.-M. and Baiker, A. (2010). Exploring catalytic solid/liquid interfaces by in situ attenuated total reflection infrared spectroscopy. *Chemical Society Reviews* 39 (12): 4571–4584.
- 25 Yang, C. and Wöll, C. (2017). IR spectroscopy applied to metal oxide surfaces: adsorbate vibrations and beyond. *Advances in Physics: X* 2 (2): 373–408.
- 26 Kortüm, G. (1969). *Reflectance Spectroscopy: Principles, Methods, Applications*. New York: Springer-Verlag.
- 27 Kortüm, G., Braun, W., and Herzog, G. (1963). Principles and Techniques of diffuse-reflectance spectroscopy. *Angewandte Chemie, International Edition* 2 (7): 333–341.
- 28 Kortüm, G. and Oelkrug, D. (1964). Über den Streukoeffizienten der Kubelka-Munk-Theorie. *Zeitschrift für Naturforschung - Section A Journal of Physical Sciences* 19 (1): 28–37.
- 29 Zeng, L. and Li, D. (2015). Development of in situ sensors for chlorophyll concentration measurement. *Journal of Sensors* 2015: 903509.
- 30 Djurišić, A.B. and Leung, Y.H. (2006). Optical properties of ZnO nanostructures. *Small* 2 (8–9): 944–961.
- 31 Lin, K.-F., Cheng, H.-M., Hsu, H.-C. et al. (2005). Band gap variation of size-controlled ZnO quantum dots synthesized by sol-gel method. *Chemical Physics Letters* 409 (4–6): 208–211.
- 32 Sternig, A., Stankic, S., Müller, M. et al. (2008). Photoluminescent nanoparticle surfaces: The potential of alkaline earth oxides for optical applications. *Advanced Materials* 20 (24): 4840–4844.
- 33 Zhang, Z. and Yates, J.T. (2012). Band bending in semiconductors: Chemical and physical consequences at surfaces and interfaces. *Chemical Reviews* 112 (10): 5520–5551.
- 34 Stevanovic, A., Büttner, M., Zhang, Z., and Yates, J.T. Jr., (2012). Photoluminescence of TiO₂: Effect of UV light and adsorbed molecules on surface band structure. *Journal of the American Chemical Society* 134 (1): 324–332.
- 35 Kisch, H. (2015). *Semiconductor Photocatalysis: Principles and Applications*. Wiley-VCH.
- 36 Poncé, S., Jia, Y., Giantomassi, M. et al. (2016). Understanding thermal quenching of photoluminescence in oxynitride phosphors from first principles. *Journal of Physical Chemistry C* 120 (7): 4040–4047.
- 37 Feldmann, C., Jüstel, T., Ronda, C.R., and Schmidt, P.J. (2003). Inorganic luminescent materials: 100 Years of research and application. *Advanced Functional Materials* 13 (7): 511–516.
- 38 Han, J.K., Choi, J.I., Piquette, A. et al. (2013). Phosphor development and integration for near-UV LED solid state lighting. *ECS Journal of Solid State Science and Technology* 2 (2): R3138–R3147.
- 39 Sternig, A., Bernardi, J., McKenna, K., and Diwald, O. (2015). Surface-specific visible light luminescence from composite metal oxide nanocrystals. *Journal of Materials Science* 50 (24): 8153–8165.
- 40 Feldmann, C. (2011). Luminescent nanomaterials. *Nanoscale* 3 (5): 1947–1948.
- 41 Bravo-Suárez, J.J. and Srinivasan, P.D. (2017). Design characteristics of in situ and operando ultraviolet-visible and vibrational spectroscopic reaction cells for heterogeneous catalysis. *Catalysis Reviews* 59 (4): 295–445.
- 42 Tsakoumis, N.E., York, A.P.E., Chen, D., and Rønning, M. (2015). Catalyst characterisation techniques and reaction cells operating at realistic conditions; towards acquisition of kinetically relevant information. *Catalysis Science and Technology* 5 (11): 4859–4883.
- 43 Melsheimer, J., Thiede, M., Ahmad, R. et al. (2003). Improved experimental setup for in situ UV-vis-NIR spectroscopy under catalytic conditions. *Physical Chemistry Chemical Physics* 5 (20): 4366–4370.

- 44 Marcelli, A., Innocenzi, P., Malfatti, L. et al. (2012). IR and X-ray time-resolved simultaneous experiments: An opportunity to investigate the dynamics of complex systems and non-equilibrium phenomena using third-generation synchrotron radiation sources. *Journal of Synchrotron Radiation* 19 (6): 892–904.
- 45 Gruene, P., Wolfram, T., Pelzer, K. et al. (2010). Role of dispersion of vanadia on SBA-15 in the oxidative dehydrogenation of propane. *Catalysis Today* 157 (1–4): 137–142.
- 46 Le, H.V., Parishan, S., Sagaltchik, A. et al. (2017). Solid-State Ion-Exchanged Cu/Mordenite Catalysts for the Direct Conversion of Methane to Methanol. *ACS Catalysis* 7 (2): 1403–1412.
- 47 Klose, B.S., Jentoft, F.C., Joshi, P. et al. (2006). In situ spectroscopic investigation of activation, start-up and deactivation of promoted sulfated zirconia catalysts. *Catalysis Today* 116 (2 SPEC. ISS), 121–131.
- 48 Srinivasan, P.D., Nitz, S.R., Stephens, K.J. et al. (2018). Modified Harrick reaction cell for in situ/operando fiber optics diffuse reflectance UV–visible spectroscopic characterization of catalysts. *Applied Catalysis A: General* 561: 7–18.
- 49 Nijhuis, T.A., Tinnemans, S.J., Visser, T., and Weckhuysen, B.M. (2003). Operando spectroscopic investigation of supported metal oxide catalysts by combined time-resolved UV-VIS/Raman/on-line mass spectrometry. *Physical Chemistry Chemical Physics* 5 (20): 4361–4365.
- 50 Borodina, E., Meirer, F., Lezcano-González, I. et al. (2015). Influence of the reaction temperature on the nature of the active and deactivating species during methanol to olefins conversion over H-SSZ-13. *ACS Catalysis* 5 (2): 992–1003.
- 51 Ovsitser, O., Cherian, M., Brückner, A., and Kondratenko, E.V. (2009). Dynamics of redox behavior of nano-sized VO_x species over Ti-Si-MCM-41 from time-resolved in situ UV/Vis analysis. *Journal of Catalysis* 265 (1): 8–18.
- 52 Risch, M., Ringleb, F., Kohlhoff, M. et al. (2015). Water oxidation by amorphous cobalt-based oxides: In situ tracking of redox transitions and mode of catalysis. *Energy and Environmental Science* 8 (2): 661–674.
- 53 Trzeźniewski, B.J., Diaz-Morales, O., Vermaas, D.A. et al. (2015). In situ observation of active oxygen species in Fe-containing Ni-based oxygen evolution catalysts: The effect of pH on electrochemical activity. *Journal of the American Chemical Society* 137 (48): 15112–15121.
- 54 Berger, T., Anta, J.A., and Morales-Flórez, V. (2012). Electrons in the band gap: Spectroscopic characterization of anatase TiO₂ nanocrystal electrodes under Fermi level control. *Journal of Physical Chemistry C* 116 (21): 11444–11455.
- 55 Woodward, P.M., Mizoguchi, H., Kim, Y.-I., and Stolfus, M.W. (2006). The electronic structure of metal oxides. In: *Metal Oxides – Chemistry and Applications, Vol. 108* (ed. J.L.G. Fierro), 133. Boca Raton: CRC Press, Taylor & Francis Group.
- 56 Suntivich, J., May, K.J., Gasteiger, H.A. et al. (2011). A perovskite oxide optimized for oxygen evolution catalysis from molecular orbital principles. *Science* 334 (6061): 1383–1385.
- 57 Thompson, T.L. and Yates, J.T. Jr., (2006). Surface science studies of the photoactivation of TiO₂ – New photochemical processes. *Chemical Reviews* 106 (10): 4428–4453.
- 58 Agrawal, A., Johns, R.W., and Milliron, D.J. (2017). Control of localized surface plasmon resonances in metal oxide nanocrystals. *Annual Review of Materials Research* 47: 1–31.
- 59 Miras, H.N., Vilà-Nadal, L., and Cronin, L. (2014). Polyoxometalate based open-frameworks (POM-OFs). *Chemical Society Reviews* 43 (16): 5679–5699.
- 60 Tilley, R.J.D. (2016). *Perovskites: Structure-Property Relationships*.
- 61 Flanigen, E.M., Bennett, J.M., Grose, R.W. et al. (1978). Silicalite, a new hydrophobic crystalline silica molecular sieve. *Nature* 271 (5645): 512–516.

- 62 Li, C., Moliner, M., and Corma, A. (2018). Building Zeolites from Precrystallized Units: Nanoscale Architecture. *Angewandte Chemie, International Edition* 57 (47): 15330–15353.
- 63 Gumerova, N.I. and Rompel, A. (2018). Synthesis, structures and applications of electron-rich polyoxometalates. *Nature Reviews Chemistry* 2: 0112.
- 64 Vilà-Nadal, L. and Cronin, L. (2017). Design and synthesis of polyoxometalate-framework materials from cluster precursors. *Nature Reviews Materials* 2: 17054.
- 65 Pope, M.T. and Müller, A. (1991). Polyoxometalate chemistry: An old field with new dimensions in several disciplines. *Angewandte Chemie, International Edition in English* 30 (1): 34–48.
- 66 Maganas, D., Trunschke, A., Schlögl, R., and Neese, F. (2016). A unified view on heterogeneous and homogeneous catalysts through a combination of spectroscopy and quantum chemistry. *Faraday Discussions* 188: 181–197.
- 67 Wachs, I.E. (2013). Catalysis science of supported vanadium oxide catalysts. *Dalton Transactions* 42 (33): 11762–11769.
- 68 Yadav, L.D.S. (ed.) (2005). In *Organic Spectroscopy*, 7. Dordrecht, Netherlands: Springer.
- 69 Kisch, H. (2013). Semiconductor photocatalysis – Mechanistic and synthetic aspects. *Angewandte Chemie, International Edition* 52 (3): 812–847.
- 70 Linsebigler, A.L., Lu, G., and Yates, J.T. (1995). Photocatalysis on TiO₂ surfaces: Principles, mechanisms, and selected results. *Chemical Reviews* 95 (3): 735–758.
- 71 Henglein, A. (1989). Small-particle research: Physicochemical properties of extremely small colloidal metal and semiconductor particles. *Chemical Reviews* 89 (8): 1861–1873.
- 72 Hagfeldt, A. and Grätzel, M. (1995). Light-Induced redox reactions in nanocrystalline systems. *Chemical Reviews* 95 (1): 49–68.
- 73 Stankic, S., Müller, M., Diwald, O. et al. (2005). Size-dependent optical properties of MgO nanocubes. *Angewandte Chemie, International Edition* 44 (31): 4917–4920.
- 74 Garrone, E., Zecchina, A., and Stone, F.S. (1980). An experimental and theoretical evaluation of surface states in MgO and other alkaline earth oxides. *Philosophical Magazine B: Physics of Condensed Matter; Statistical Mechanics, Electronic, Optical and Magnetic Properties* 42 (5): 683–703.
- 75 Müller, M., Stankic, S., Diwald, O. et al. (2007). Effect of protons on the optical properties of oxide nanostructures. *Journal of the American Chemical Society* 129 (41): 12491–12496.
- 76 Schneider, J., Franke, M., Gurrath, M. et al. (2016). Porphyrin metalation at MgO surfaces: A spectroscopic and quantum mechanical study on complementary model systems. *Chemistry – A European Journal* 22 (5): 1744–1749.
- 77 Wulfers, M.J. and Jentoft, F.C. (2013). Identification of carbonaceous deposits formed on H-mordenite during alkane isomerization. *Journal of Catalysis* 307: 204–213.
- 78 Yarulina, I., Chowdhury, A.D., Meirer, F. et al. (2018). Recent trends and fundamental insights in the methanol-to-hydrocarbons process. *Nature Catalysis* 1 (6): 398–411.
- 79 Hunger, M. (2005). Applications of in situ spectroscopy in zeolite catalysis. *Microporous and Mesoporous Materials* 82 (3): 241–255.
- 80 Ballhausen, C.J. (1977). Approximate methods for the electronic structures of inorganic complexes. In: *Semiempirical Methods of Electronic Structure Calculation: Part B: Applications* (ed. G.A. Segal), 129–162. Boston, MA: Springer US.
- 81 Singh, S.K., Eng, J., Atanasov, M., and Neese, F. (2017). Covalency and chemical bonding in transition metal complexes: An ab initio based ligand field perspective. *Coordination Chemistry Reviews* 344: 2–25.
- 82 El-Sayed, M.A. (2001). Some interesting properties of metals confined in time and nanometer space of different shapes. *Accounts of Chemical Research* 34 (4): 257–264.

- 83 Kelly, K.L., Coronado, E., Zhao, L.L., and Schatz, G.C. (2003). The optical properties of metal nanoparticles: The influence of size, shape, and dielectric environment. *Journal of Physical Chemistry B* 107 (3): 668–677.
- 84 Creighton, J.A. and Eadon, D.G. (1991). Ultraviolet-visible absorption spectra of the colloidal metallic elements. *Journal of the Chemical Society, Faraday Transactions* 87 (24): 3881–3891.
- 85 Khlebtsov, B.N. and Khlebtsov, N.G. (2007). Multipole plasmons in metal nanorods: Scaling properties and dependence on particle size, shape, orientation, and dielectric environment. *Journal of Physical Chemistry C* 111 (31): 11516–11527.
- 86 Liu, L. and Corma, A. (2018). Metal catalysts for heterogeneous catalysis: From single atoms to nanoclusters and nanoparticles. *Chemical Reviews* 118 (10): 4981–5079.
- 87 El-Sayed, I.H., Huang, X., and El-Sayed, M.A. (2005). Surface plasmon resonance scattering and absorption of anti-EGFR antibody conjugated gold nanoparticles in cancer diagnostics: Applications in oral cancer. *Nano Letters* 5 (5): 829–834.
- 88 Morton, S.M., Silverstein, D.W., and Jensen, L. (2011). Theoretical studies of plasmonics using electronic structure methods. *Chemical Reviews* 111 (6): 3962–3994.
- 89 Pankove, J.I. (1971). *Optical Processes in Semiconductors*. Dover Publications.
- 90 Basu, P.K. (1997). *Theory of Optical Processes in Semiconductors*. Oxford University Press.
- 91 Szczepankiewicz, S.H., Moss, J.A., and Hoffmann, M.R. (2002). Slow surface charge trapping kinetics on irradiated TiO₂. *Journal of Physical Chemistry B* 106 (11): 2922–2927.
- 92 Berger, T., Sterrer, M., Diwald, O. et al. (2005). Light-induced charge separation in anatase TiO₂ particles. *Journal of Physical Chemistry B* 109 (13): 6061–6068.
- 93 Panayotov, D.A., Burrows, S.P., Yates, J.T., and Morris, J.R. (2011). Mechanistic studies of hydrogen dissociation and spillover on Au/TiO₂: IR spectroscopy of coadsorbed CO and H-donated electrons. *Journal of Physical Chemistry C* 115 (45): 22400–22408.
- 94 Noei, H., Qiu, H., Wang, Y. et al. (2010). Hydrogen loading of oxide powder particles: A transmission IR study for the case of zinc oxide. *ChemPhysChem* 11 (17): 3604–3607.
- 95 Takeuchi, M., Martra, G., Coluccia, S., and Anpo, M. (2005). Investigations of the structure of H₂O clusters adsorbed on TiO₂ surfaces by near-infrared absorption spectroscopy. *Journal of Physical Chemistry B* 109 (15): 7387–7391.
- 96 Ye, X., Fei, J., Diroll, B.T. et al. (2014). Expanding the spectral tunability of plasmonic resonances in doped metal-oxide nanocrystals through cooperative cation-anion codoping. *Journal of the American Chemical Society* 136 (33): 11680–11686.
- 97 Celaya Sanfiz, A., Hansen, T.W., Girgsdies, F. et al. (2008). Preparation of phase-pure M1 MoVTenb oxide catalysts by hydrothermal synthesis – Influence of reaction parameters on structure and morphology. *Topics in Catalysis* 50 (1-4): 19–32.
- 98 Canioni, R., Marchal-Roch, C., Leclerc-Laronze, N. et al. (2011). Selective conversion of {Mo₁₃₂} Keplerate ion into 4-electron reduced crown-capped Keggin derivative [Te₅Mo₁₅O₅₇]⁸⁻. A key intermediate to single-phase M1 multielement MoVTenO light-alkanes oxidation catalyst. *Chemical Communications* 47 (22): 6413–6415.
- 99 Espinosa-Alonso, L., Beale, A.M., and Weckhuysen, B.M. (2010). Profiling physicochemical changes within catalyst bodies during preparation: New insights from invasive and noninvasive microspectroscopic studies. *Accounts of Chemical Research* 43 (9): 1279–1288.
- 100 Zander, S., Seidlhofer, B., and Behrens, M. (2012). In situ EDXRD study of the chemistry of aging of co-precipitated mixed Cu,Zn hydroxycarbonates – Consequences for the preparation of Cu/ZnO catalysts. *Dalton Transactions* 41 (43): 13413–13422.
- 101 Gao, X., Bare, S.R., Weckhuysen, B.M., and Wachs, I.E. (1998). In situ spectroscopic investigation of molecular structures of highly dispersed vanadiumoxide on silica under various conditions. *Journal of Physical Chemistry B* 102 (52): 10842–10852.

- 102** Sojka, Z., Bozon-Verduraz, F., and Che, M. (2008). UV-VIS-NIR and EPR spectroscopies. In: *Handbook of Heterogeneous Catalysis*, (eds. G. Ertl, H. Knözinger, and J. Weitkamp), 1039–1064. Wiley-VCH.
- 103** Grundner, S., Markovits, M.A.C., Li, G. et al. (2015). Single-site trinuclear copper oxygen clusters in mordenite for selective conversion of methane to methanol. *Nature Communications* 6: 7546.
- 104** Wulfers, M.J., Teketel, S., Ipek, B., and Lobo, R.F. (2015). Conversion of methane to methanol on copper-containing small-pore zeolites and zeotypes. *Chemical Communications* 51 (21): 4447–4450.
- 105** Vanelderden, P., Snyder, B.E.R., Tsai, M.-L. et al. (2015). Spectroscopic definition of the copper active sites in mordenite: Selective methane oxidation. *Journal of the American Chemical Society* 137 (19): 6383–6392.
- 106** Giordanino, F., Vennestrøm, P.N.R., Lundegaard, L.F. et al. (2013). Characterization of Cu-exchanged SSZ-13: A comparative FTIR, UV-Vis, and EPR study with Cu-ZSM-5 and Cu- β with similar Si/Al and Cu/Al ratios. *Dalton Transactions* 42 (35): 12741–12761.
- 107** Bordiga, S., Bonino, F., Damin, A., and Lamberti, C. (2007). Reactivity of Ti(IV) species hosted in TS-1 towards H₂O₂-H₂O solutions investigated by ab initio cluster and periodic approaches combined with experimental XANES and EXAFS data: A review and new highlights. *Physical Chemistry Chemical Physics* 9 (35): 4854–4878.
- 108** Bobadilla, L.F., Santos, J.L., Ivanova, S. et al. (2018). Unravelling the role of oxygen vacancies in the mechanism of the reverse water-gas shift reaction by operando DRIFTS and ultraviolet-visible spectroscopy. *ACS Catalysis* 8 (8): 7455–7467.
- 109** Piovano, A., Morra, E., Chiesa, M., and Groppo, E. (2017). Tuning the Ti³⁺ and Al³⁺ synergy in an Al₂O₃/TiCl_x catalyst to modulate the grade of the produced polyethylene. *ACS Catalysis* 7 (8): 4915–4921.
- 110** Kondratenko, E.V., Takahashi, N., Nagata, N. et al. (2015). Operando UV/Vis analysis of the synergy effect between copper and gold in nitric oxide reduction over gold and copper on alumina catalysts. *ChemCatChem* 7 (23): 3956–3962.
- 111** Oord, R., Schmidt, J.E., and Weckhuysen, B.M. (2018). Methane-to-methanol conversion over zeolite Cu-SSZ-13, and its comparison with the selective catalytic reduction of NO_x with NH₃. *Catalysis Science and Technology* 8 (4): 1028–1038.
- 112** Rout, K.R., Fenes, E., Baidoo, M.F. et al. (2016). Highly active and stable CeO₂-promoted CuCl₂/Al₂O₃ oxychlorination catalysts developed by rational design using a rate diagram of the catalytic cycle. *ACS Catalysis* 6 (10): 7030–7039.
- 113** Zabilskiy, M., Djinović, P., Tchernychova, E., and Pintar, A. (2016). N₂O decomposition over CuO/CeO₂ catalyst: New insights into reaction mechanism and inhibiting action of H₂O and NO by operando techniques. *Applied Catalysis B: Environmental* 197: 146–158.
- 114** Gorlin, M., de Araujo, J.F., Schmies, H. et al. (2017). Tracking catalyst redox states and reaction dynamics in Ni-Fe oxyhydroxide oxygen evolution reaction electrocatalysts: The role of catalyst support and electrolyte pH. *Journal of the American Chemical Society* 139 (5): 2070–2082.
- 115** Chakrabarti, A., Gierada, M., Handzlik, J., and Wachs, I.E. (2016). Operando Molecular spectroscopy during ethylene polymerization by supported CrO_x/SiO₂ catalysts: Active sites, reaction intermediates, and structure-activity relationship. *Topics in Catalysis* 59 (8-9): 725–739.
- 116** Rosser, T.E. and Reisner, E. (2017). Understanding Immobilized molecular catalysts for fuel-forming reactions through UV/Vis spectroelectrochemistry. *ACS Catalysis* 7 (5): 3131–3141.

- 117 Bañares, M.A. (2005). Operando methodology: Combination of in situ spectroscopy and simultaneous activity measurements under catalytic reaction conditions. *Catalysis Today* 100 (1-2): 71–77.
- 118 Chakrabarti, A., Ford, M.E., Gregory, D. et al. (2017). A decade of operando spectroscopy studies. *Catalysis Today* 283: 27–53.
- 119 Sattler, J.J.H.B., González-Jiménez, I.D., Mens, A.M. et al. (2013). Operando UV-Vis spectroscopy of a catalytic solid in a pilot-scale reactor: Deactivation of a $\text{CrO}_x/\text{Al}_2\text{O}_3$ propane dehydrogenation catalyst. *Chemical Communications* 49 (15): 1518–1520.
- 120 Jiang, Y., Huang, J., Reddy Marthala, V.R. et al. (2007). In situ MAS NMR-UV/Vis investigation of H-SAPO-34 catalysts partially coked in the methanol-to-olefin conversion under continuous-flow conditions and of their regeneration. *Microporous and Mesoporous Materials* 105 (1–2): 132–139.
- 121 Olsbye, U., Svelle, S., Bjrgen, M. et al. (2012). Conversion of methanol to hydrocarbons: How zeolite cavity and pore size controls product selectivity. *Angewandte Chemie, International Edition* 51 (24): 5810–5831.
- 122 Goetze, J. and Weckhuysen, B.M. (2018). Spatiotemporal coke formation over zeolite ZSM-5 during the methanol-to-olefins process as studied with: Operando UV-vis spectroscopy: A comparison between H-ZSM-5 and Mg-ZSM-5. *Catalysis Science and Technology* 8 (6): 1632–1644.
- 123 Vogt, C., Weckhuysen, B.M., and Ruiz-Martínez, J. (2017). Effect of feedstock and catalyst impurities on the methanol-to-olefin reaction over H-SAPO-34. *ChemCatChem* 9 (1): 183–194.
- 124 Amakawa, K., Sun, L., Guo, C. et al. (2013). How strain affects the reactivity of surface metal oxide catalysts. *Angewandte Chemie, International Edition* 52 (51): 13553–13557.
- 125 Kubas, A., Noak, J., Trunschke, A. et al. (2017). A combined experimental and theoretical spectroscopic protocol for determination of the structure of heterogeneous catalysts: Developing the information content of the resonance Raman spectra of M1 MoVO_x . *Chemical Science* 8 (9): 6338–6353.
- 126 Klokishner, S., Reu, O., Tzolova-Müller, G. et al. (2014). Apparent absorption spectra of silica supported vanadium-titanium oxide catalysts: Experimental study and modeling. *Journal of Physical Chemistry C* 118 (26): 14677–14691.
- 127 Klokishner, S., Reu, O., Noack, J. et al. (2017). Experimental study and modeling of the UV-Vis and infrared spectra of the $[\text{VO}(\text{O}_2)\text{Hheida}]$ - complex dissolved in water. *Journal of Physical Chemistry A* 121 (38): 7157–7164.
- 128 Maganas, D., Roemelt, M., Hävecker, M. et al. (2013). First principles calculations of the structure and V L-edge X-ray absorption spectra of V_2O_5 using local pair natural orbital coupled cluster theory and spin-orbit coupled configuration interaction approaches. *Physical Chemistry Chemical Physics* 15 (19): 7260–7276.
- 129 Barton, D.G., Shtein, M., Wilson, R.D. et al. (1999). Structure and electronic properties of solid acids based on tungsten oxide nanostructures. *Journal of Physical Chemistry B* 103 (4): 630–640.
- 130 Chen, K., Bell, A.T., and Iglesia, E. (2002). The relationship between the electronic and redox properties of dispersed metal oxides and their turnover rates in oxidative dehydrogenation reactions. *Journal of Catalysis* 209 (1): 35–42.
- 131 Gao, X. and Wachs, I.E. (2000). Investigation of surface structures of supported vanadium oxide catalysts by UV-vis-NIR diffuse reflectance spectroscopy. *Journal of Physical Chemistry B* 104 (6): 1261–1268.

- 132** Tabacchi, G., Gianotti, E., Fois, E. et al. (2007). Understanding the vibrational and electronic features of Ti(IV) sites in mesoporous silicas by integrated ab initio and spectroscopic investigations. *Journal of Physical Chemistry C* 111 (13): 4946–4955.
- 133** Hamilton, N., Wolfram, T., Tzolova Müller, G. et al. (2012). Topology of silica supported vanadium-titanium oxide catalysts for oxidative dehydrogenation of propane. *Catalysis Science and Technology* 2 (7): 1346–1359.
- 134** Neese, F. (2012). The ORCA program system. *Wiley Interdisciplinary Reviews: Computational Molecular Science* 2 (1): 73–78.
- 135** Goetze, J., Yarulina, I., Gascon, J. et al. (2018). Revealing lattice expansion of small-pore zeolite catalysts during the methanol-to-olefins process using combined operando X-ray diffraction and UV-vis spectroscopy. *ACS Catalysis* 8 (3): 2060–2070.
- 136** Gomez-Romero, P. and Sanchez, C. (2004). *Functional Hybrid Materials*. Wiley-VCH.
- 137** Mills, A. and Wells, N. (2015). Reductive photocatalysis and smart inks. *Chemical Society Reviews* 44 (10): 2849–2864.
- 138** Wang, W., Xie, N., He, L., and Yin, Y. (2014). Photocatalytic colour switching of redox dyes for ink-free light-printable rewritable paper. *Nature Communications* 5: 5459.
- 139** Hagfeldt, A., Boschloo, G., Sun, L. et al. (2010). Dye-sensitized solar cells. *Chemical Reviews* 110 (11): 6595–6663.
- 140** Xu, P., McCool, N.S., and Mallouk, T.E. (2017). Water splitting dye-sensitized solar cells. *Nano Today* 14: 42–58.
- 141** Urbani, M., Grätzel, M., Nazeeruddin, M.K., and Torres, T. (2014). Meso-substituted porphyrins for dye-sensitized solar cells. *Chemical Reviews* 114 (24): 12330–12396.
- 142** Gouterman, M. (1959). Study of the effects of substitution on the absorption spectra of porphyrin. *The Journal of Chemical Physics* 30 (5): 1139–1161.
- 143** Barraud, E. (2013). Stained glass solar windows for the swiss tech convention center. *Chimia* 67 (3): 181–182.
- 144** Zhang, L. and Cole, J.M. (2015). Anchoring groups for dye-sensitized solar cells. *ACS Applied Materials and Interfaces* 7 (6): 3427–3455.
- 145** Zhang, L. and Cole, J.M. (2017). Dye aggregation in dye-sensitized solar cells. *Journal of Materials Chemistry A* 5 (37): 19541–19559.
- 146** Rochford, J., Chu, D., Hagfeldt, A., and Galoppini, E. (2007). Tetrachelate porphyrin chromophores for metal oxide semiconductor sensitization: Effect of the spacer length and anchoring group position. *Journal of the American Chemical Society* 129 (15): 4655–4665.
- 147** Berger, T. and Diwald, O. (2015). Defects in metal oxide nanoparticle powders. In: *Defects at Oxide Surfaces* (J. Jupille and G. Thornton), 273–301. Springer.
- 148** Schneider, J., Kollhoff, F., Bernardi, J. et al. (2015). Porphyrin metalation at the MgO nanocube/toluene interface. *ACS Applied Materials and Interfaces* 7 (41): 22962–22969.
- 149** Schneider, J., Kollhoff, F., Schindler, T. et al. (2016). Adsorption, ordering, and metalation of porphyrins on MgO nanocube surfaces: The directional role of carboxylic anchoring groups. *Journal of Physical Chemistry C* 120 (47): 26879–26888.
- 150** Knözinger, E., Diwald, O., and Sterrer, M. (2000). Chemical vapour deposition – A new approach to reactive surface defects of uniform geometry on high surface area magnesium oxide. *Journal of Molecular Catalysis A: Chemical* 162 (1-2): 83–95.
- 151** Baumann, S.O., Schneider, J., Sternig, A. et al. (2015). Size effects in MgO cube dissolution. *Langmuir* 31 (9): 2770–2776.

- 152 Edwards, L., Dolphin, D.H., Gouterman, M., and Adler, A.D. (1971). Porphyrins XVII. Vapor absorption spectra and redox reactions: Tetraphenylporphins and porphin. *Journal of Molecular Spectroscopy* 38 (1): 16–32.
- 153 Rubio, M., Roos, B.O., Serrano-Andrés, L., and Merchán, M. (1999). Theoretical study of the electronic spectrum of magnesium-porphyrin. *Journal of Chemical Physics* 110 (15): 7202–7209.
- 154 Sternig, A., Stankic, S., Müller, M. et al. (2012). Surface exciton separation in photoexcited MgO nanocube powders. *Nanoscale* 4 (23): 7494–7500.
- 155 Makuła, P., Pacia, M., Macyk, W. (2018). How to correctly determine the band gap energy of modified semiconductor photocatalysts based on UV-Vis spectra. *Journal of Physical Chemistry Letters* 9: 6814–6817.